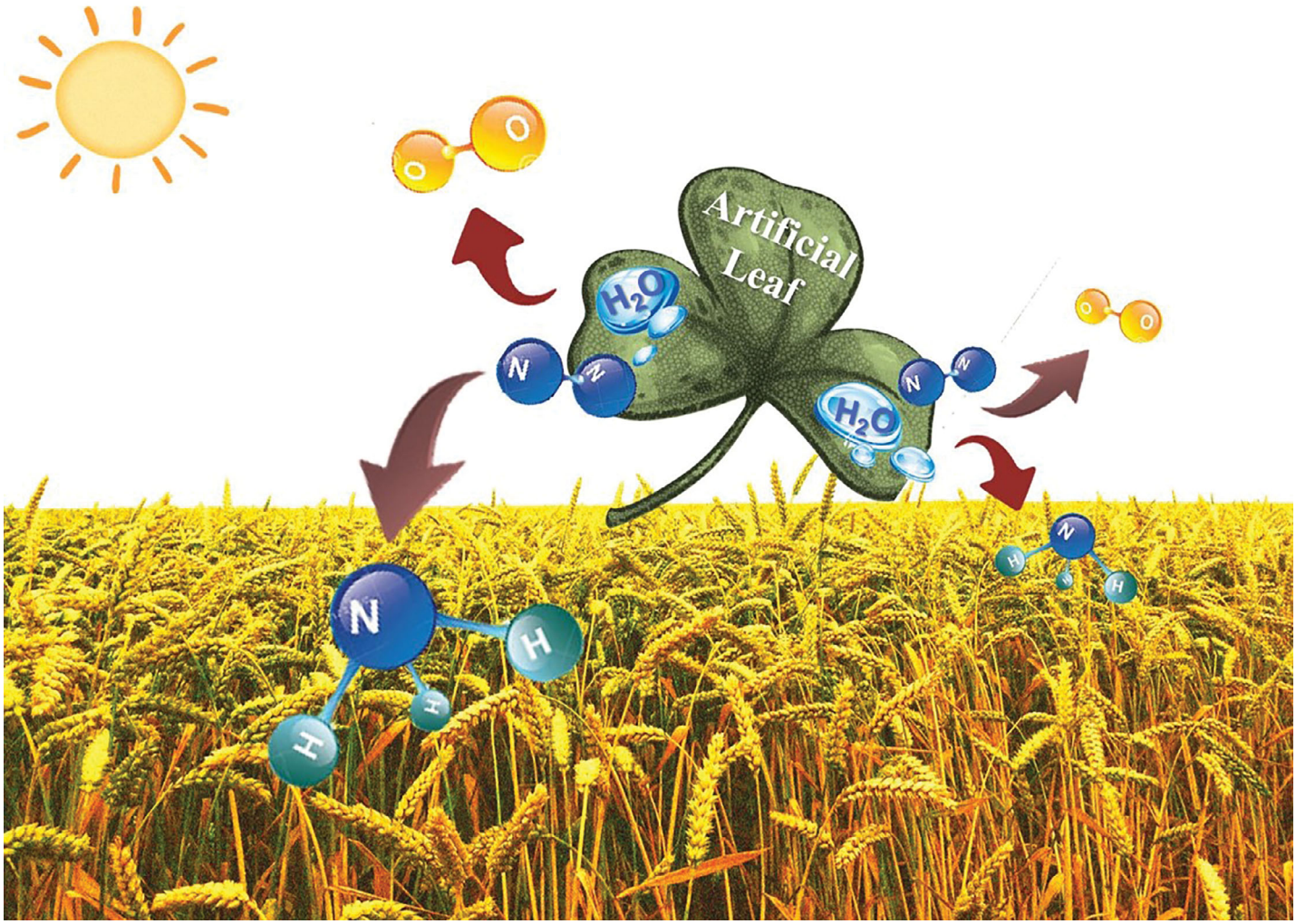

Showcasing research from Professor Junwang Tang's laboratory, Department of Chemical Engineering, University College London, London, United Kingdom.

Progress and challenges in photocatalytic ammonia synthesis

The group of Solar Energy and Advanced Materials, led by Prof. Junwang Tang focuses on photocatalytic small molecule activation (including CH_4, N_2, H_2O, C_6H_6 and CO_2) to high-value chemicals/fuels and microwave catalysis (*e.g.* plastic chemical recycling), together with microwave-intensified chemical processes. In parallel, the group has state-of-the-art spectroscopies to investigate the underlying charge dynamics and kinetics. This review puts forward a few critical issues existing in nitrogen photoreduction, along with a comprehensive discussion of strategies for improvement of NH_3 yield, aiming to make substantial contribution towards advancing this field.

As featured in:

See Junwang Tang *et al.*, *Mater. Adv.*, 2021, **2**, 564.

ROYAL SOCIETY OF CHEMISTRY

rsc.li/materials-advances

Registered charity number: 207890

Materials Advances

ROYAL SOCIETY OF CHEMISTRY

REVIEW

View Article Online
View Journal | View Issue

Check for updates

Cite this: *Mater. Adv.*, 2021, **2**, 564

Progress and challenges in photocatalytic ammonia synthesis

Qing Han, †[ab] Haimiao Jiao, †[b] Lunqiao Xiong [b] and Junwang Tang *[b]

Photocatalytic ammonia (NH_3) synthesis from N_2 and water driven by solar energy is a sustainable and environmentally friendly technology, which has gained considerable attention in recent years. In this review, the recent development in the fundamental understanding of photocatalytic NH_3 synthesis and the methods of precise NH_3 detection are summarized. More importantly the strategy for surface engineering and interface engineering of photocatalysts toward photocatalytic NH_3 production has been thoroughly analyzed with the aim to stimulate critical thinking about the effective methodology for catalyst modification instead of exploring new materials. At the end the challenges and a few concerns are raised from the current reports and future perspectives in this research field are discussed targeting to clarify the reliability and reproducibility of the photochemical process and to direct the future research direction, such as flow reactor design and in-depth understanding of the underlying reaction pathway.

Received 10th August 2020,
Accepted 1st November 2020

DOI: 10.1039/d0ma00590h

rsc.li/materials-advances

Open Access Article. Published on 03 11 2020. Downloaded on 2025-03-11 5:25:41.
This article is licensed under a Creative Commons Attribution 3.0 Unported Licence.

Introduction

Ammonia (NH_3) has been regarded as one of the most important chemical products as feedstock for fertilizers and for various chemicals.[1,2] The production of NH_3 plays a prominent role in global economy with an annual yield of more than 200 million tons.[3] The industrial synthesis of NH_3 is dominated by the revolutionary Haber–Bosch process, in which pure H_2 and N_2 are reacted under high pressure at high temperature over Fe-based catalysts, which consumes 1–2% of total global fossil fuels and releases around 300 million tons of planet-warming CO_2 into the atmosphere annually.[4–7] The development of environmentally friendly, sustainable strategies with high efficiency of NH_3 production under mild conditions is highly desirable but challenging.

Currently, there are a few green routes reported for ammonia synthesis. One is biological nitrogen fixation which mostly relies on diazotrophs in nature.[8] Another one is electrochemical reduction of N_2, which uses electricity to produce NH_3.[9,10] Compared with the stringent conditions of biological nitrogen fixation and the requirement of highly conductive electrolytes

[a] *Key Laboratory of Cluster Science, Ministry of Education of China, Key Laboratory of Photoelectronic/Electrophotonic Conversion Materials, School of Chemistry and Chemical Engineering, Beijing Institute of Technology, Beijing 100081, China*
[b] *Department of Chemical Engineering, University College London, London WC1E 7JE, UK. E-mail: junwang.tang@ucl.ac.uk*
† Co-first authors: These authors contributed equally to this work.

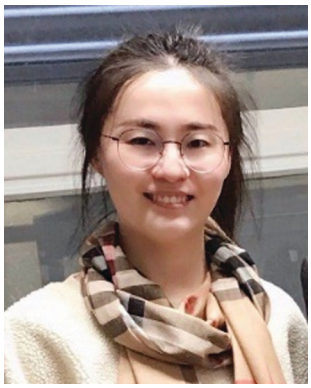

Qing Han

Qing Han is an Assistant Professor of Chemistry at Beijing Institute of Technology (Beijing, China). She received her PhD in chemistry from Beijing Institute of Technology. Her research focuses on (i) the design and synthesis of nanocatalysts for photocatalysis and electrocatalysis, and (ii) device fabrication of carbon-based nanomaterials for energy conversion.

Haimiao Jiao

Haimiao Jiao received his BEng and MSc in Chemical Engineering from Tianjin University and Imperial College London, respectively. Currently, he is a PhD student in Prof. Junwang Tang's group at the Department of Chemical Engineering, University College London. His research interests focus on photocatalytic hydrogen production from methanol and nitrogen reduction.

© 2021 The Author(s). Published by the Royal Society of Chemistry

Open Access Article. Published on 03 11 2020. Downloaded on 2025-03-11 5:25:41.
This article is licensed under a Creative Commons Attribution 3.0 Unported Licence.

and costly electrodes used in electrochemical reduction of N_2, photocatalytic ammonia synthesis using sustainable solar energy operated under either aqueous or gaseous conditions is rather different, maybe also economical, from the other methods. If the efficiency of solar driven NH_3 synthesis could be dramatically improved, this method has strong potential to replace the current Haber–Bosch process. Photocatalytic reduction of N_2 to produce NH_3 by utilizing photocatalysts and water, driven by renewable solar energy, has huge potential, and thereby is very significant.[11–17] Since the seminal work of Schrauzer and Guth in 1977,[17] in which the potential of the TiO_2 photocatalyst for N_2 reduction with water and N_2 was revealed, various semiconductors have been studied for the photocatalytic production of NH_3, such as ZnO, Fe_2O_3, Ga_2O_3, $W_{18}O_{49}$, BiOBr, BiOCl, CdS, layered double hydroxides, polymeric carbon nitride and so on.[18–25] The main challenges for the photocatalytic synthesis of NH_3 are the chemical adsorption and activation of N_2. To boost the efficiency of NH_3 photosynthesis, the exploitation of highly active photocatalytic materials is crucial. Through surface/interface engineering of various photocatalysts, the photocatalytic reaction pathways can be modulated, therefore enhancing the N_2 reduction reaction activity.

Complementary to other reviews in which different photocatalysts are summarized,[6,13,18,19,22] this crucial review tries to avoid simply listing a large population of materials and mainly concentrates on recent advances and understanding in two fast moving areas, *i.e.* surface engineering and interface engineering, which have been proved to be efficient strategies to improve most photocatalysts' activity for NH_3 synthesis, including defect engineering, morphology engineering, cocatalyst loading, and junction structure. The materials stated here are representative and highly efficient. Thus, this review aims at providing a comprehensive understanding of the rational design of highly efficient photocatalysts for N_2 photoreduction. Apart from this, the recent understanding of the photocatalytic mechanism of NH_3 synthesis and the methods to precisely evaluate the catalytic performance of a photocatalyst in NH_3 synthesis will be discussed. Future research directions for further development of the photocatalytic synthesis of NH_3 and some concerns will be highlighted at the end.

Photocatalytic mechanism of NH_3 synthesis

By mimicking the natural process of photosynthesis, researchers intend to convert solar energy, N_2 and water to NH_3 by using photocatalysts. The overall reaction is listed as follows:

$$2N_2 + 6H_2O \rightarrow 4NH_3 + 3O_2$$

In this artificial photosynthesis, there are two interlinked conversion processes, water splitting and N_2 reduction reaction (NRR).[26] As shown in Fig. 1a, upon light irradiation, photoinduced electrons generated from photocatalysts populate the conduction band, leaving holes in the valence band. Subsequently, the escaped electrons diffuse across to the reactive sites on the surface of photocatalysts. The adsorbed N_2 and H_2O are catalyzed by these electrons and holes into NH_3 and O_2, respectively, along with the generation of the byproduct H_2. Thus the key point for this process is not only to design a highly active photocatalyst but also to achieve high selectivity to NH_3 instead of H_2 gas as indicated in Fig. 1a.

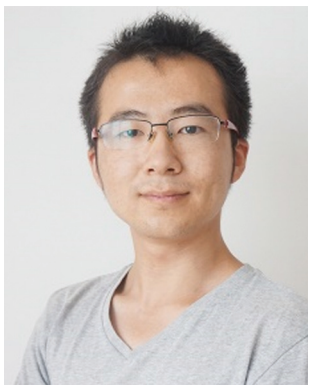

Lunqiao Xiong

Lunqiao Xiong received his BSc and MEng in Materials Science from Xi'an Jiaotong University and Tsinghua University, respectively. At present, he is a PhD student in Prof. Junwang Tang's group at the UCL Department of Chemical Engineering. His current research focuses on photocatalytic selective oxidation.

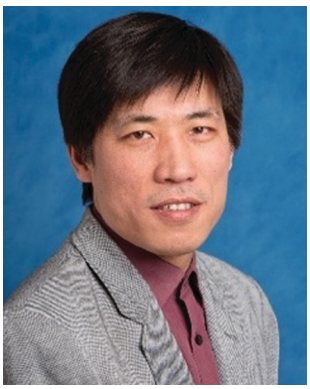

Junwang Tang

Junwang Tang is a Fellow of European Academy of Sciences, Fellow of the Royal Society of Chemistry and Professor of Materials Chemistry and Engineering in the Department of Chemical Engineering at University College London. His research interests encompass photocatalytic small molecule activation (e.g. CH_4, N_2, H_2O, CO_2 and C_6H_6) and microwave catalysis (plastic chemical recycling), together with microwave-intensified chemical processes. He has also received many awards, the latest of which is the IChemE Business Start-Up Award 2019. He also sits on the editorial/advisory board of several international journals, e.g. the Editor of Applied Catalysis B, Editor-in-Chief of Journal of Advanced Chemical Engineering, and Associate Editor of Chin. J. Catal. and Asia-Pacific Journal of Chemical Engineering.

Open Access Article. Published on 03 11 2020. Downloaded on 2025-03-11 5:25:41.
This article is licensed under a Creative Commons Attribution 3.0 Unported Licence.

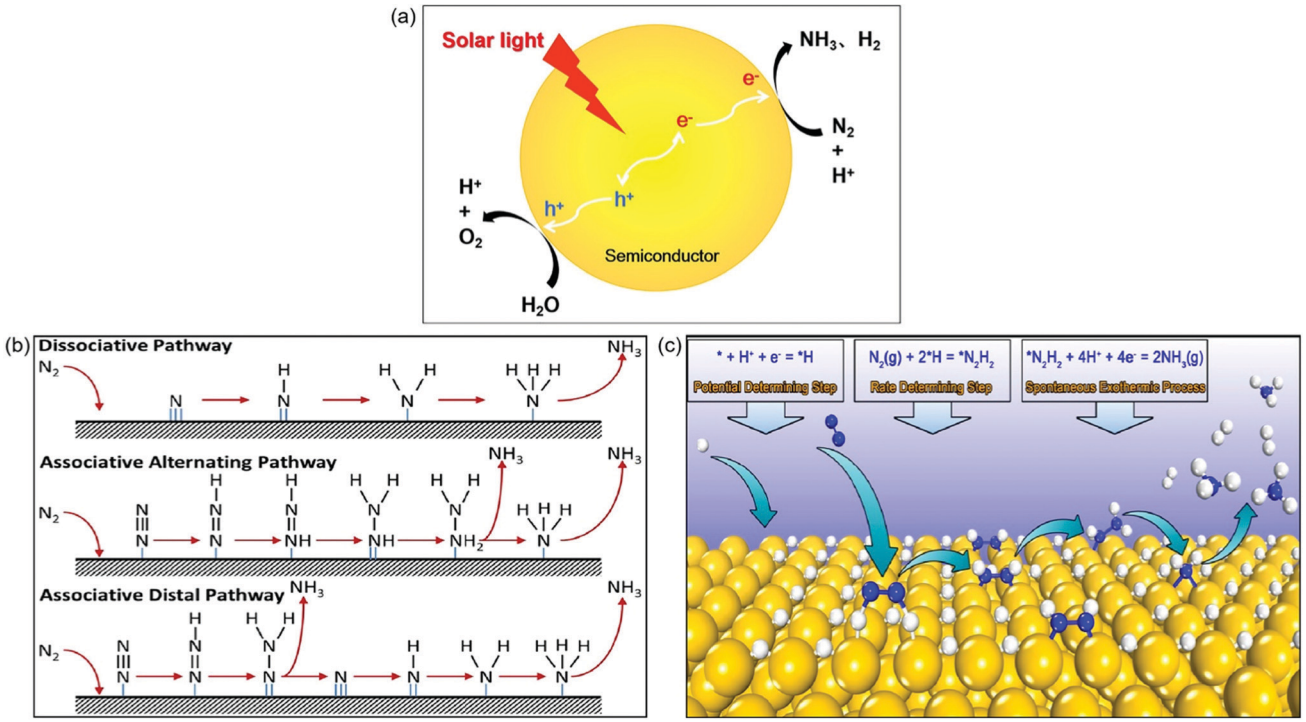

Fig. 1 (a) Photocatalytic synthesis of NH_3 in water. (b) The proposed mechanisms for photocatalytic N_2 reduction consisting of the dissociative pathway, the associative alternating pathway, and the associative distal pathway. Reproduced from ref. 27 with permission from ACS Publication. (c) The proposed mechanism of surface-hydrogenation over noble metal doped photocatalysts for NRR. Reproduced from ref. 28 with permission from ACS Publication.

Up to now, the mechanisms for N_2 reduction to NH_3 on photocatalysts have been divided into two categories based on the surface adsorption characteristics of catalysts: *N*-hydrogenation (Fig. 1b) and surface-hydrogenation (Fig. 1c).[27,28] For the *N*-hydrogenation mechanism, there are two different pathways for NRR, dissociative and associative pathways. In the dissociative pathway, the N_2 triple bond is broken before hydrogenation, followed by hydrogenation of the N-adatoms into NH_3 on the catalyst surface. The Haber–Bosch process is proved to be the dissociative pathway, which requires prohibitively high energy to cleave the N≡N bond. Compared with the dissociative pathway, the associative pathway without the breaking of the N≡N bond is generally used and accepted far more in the photocatalytic NRR. The nitrogen surface adsorption configuration determines the associative pathways for NRR; as shown in Fig. 1b, the hydrogenation of the adsorbed N_2 preferentially occurs at the terminal-site N owing to its relatively low steric hindrance for both the associative alternative pathway and the associative distal pathway. Having generated the first NH_3, the other N begins a new hydrogenation circulation to produce a second NH_3. It is actually impossible to identify the N_2 configurations due to the fact that they are favored equally by the catalysts.

Recently, a novel surface-hydrogenation mechanism for NRR has been proposed (Fig. 1c),[28] in which the adsorbed H^+ is reduced into *H first, and then N_2 molecules react with surface *H to generate $*N_2H_2$, and finally the formed $*N_2H_2$ intermediates are reduced into NH_3. The first step is the trigger step, which enables the NRR to occur at a low potential. Furthermore, the second step is the rate determining step because it needs to conquer a high energy barrier (E_a) to break the N≡N bond. The E_a of hydrogen evolution reaction is always lower than that of NRR, and therefore the NH_3 production rate is relatively low.

As a complete cycle indicated in Fig. 1a is the ideal process but very challenging, in most cases (or in the majority of the reported cases), a half reaction was investigated in which N_2 was reduced to NH_3 in the presence of an efficient hole scavenger which was oxidized other than water oxidation. This half reaction is relatively easy and can be used to preliminarily scan different photocatalysts for N_2 reduction. Bear in mind that this half reaction has advantages but does not indicate whether the photocatalyst selected is good for a complete cycle as indicated in Fig. 1a. The subsequent discussion will underline this in order to remind the audience of the large difference between a half reaction and the complete cycle.

Determination of NH_3

NH_3 detection is a necessary subject for the photocatalytic synthesis of NH_3, which is of great significance in the design of high performance photocatalysts. There are four common methods of NH_3 analysis such as colorimetric assays, ^{15}N

© 2021 The Author(s). Published by the Royal Society of Chemistry

Open Access Article. Published on 03 11 2020. Downloaded on 2025-03-11 5:25:41.
This article is licensed under a Creative Commons Attribution 3.0 Unported Licence.

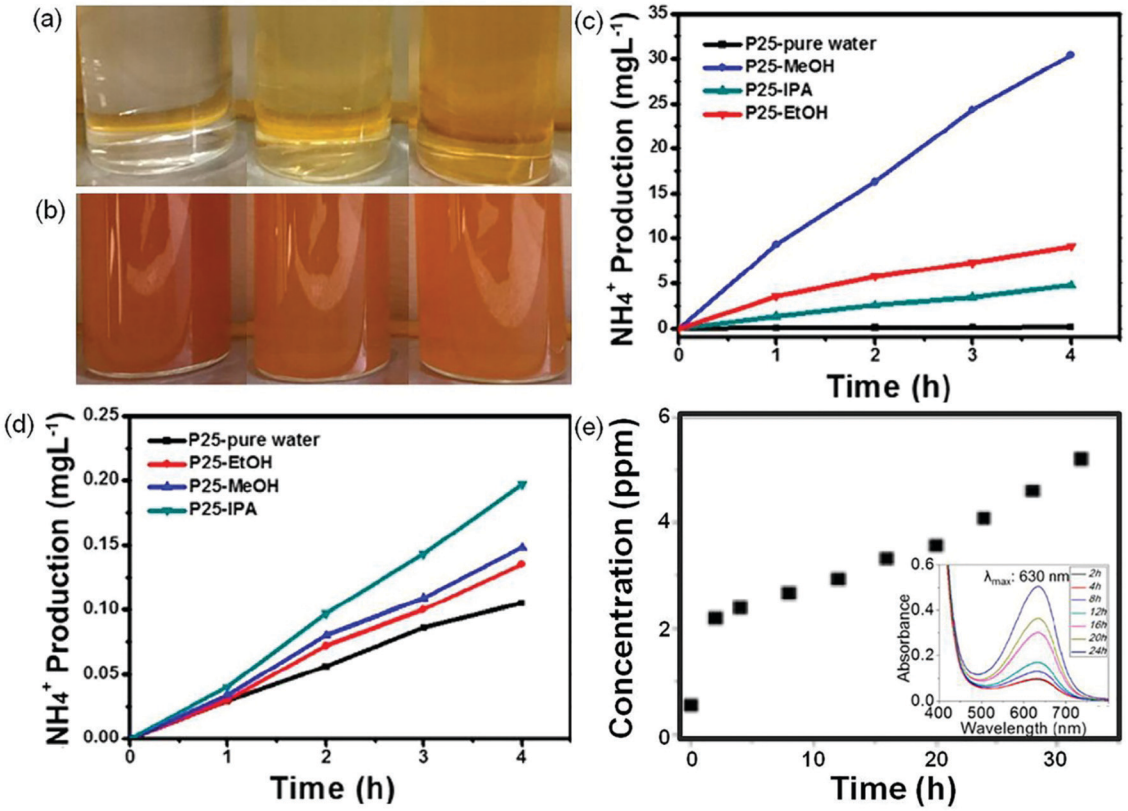

Fig. 2 Photographs of NH_3 solution with different concentrations (0, 1.2, and 4 mg L^{-1} from left to right) when (a) mixing with Nessler's reagent and (b) adding 4 μg L^{-1} formaldehyde into the above ammonia solution with Nessler's reagent. Measured results of NH_3 concentration using (c) Nessler's reagent and d) ion chromatography methods. Reproduced from ref. 29 with permission from ACS Publication. (e) The NH_3 concentration evolution with time tested by ion chromatography. Inset in (e): UV-vis absorption spectra tested with the indophenol reagent with the characteristic adsorption peak of 630 nm wavelength. Reproduced from ref. 30 with permission from ACS Publication.

isotope labeling, ion chromatography, and *in situ* infrared spectroscopic measurements.[12] The colorimetric assays include Nessler, phenate, and indophenol blue tests for NH_3 detection. Among the colorimetric assays, Nessler's reagent has been widely used in NH_3 detection due to its advantages of simplicity and low cost.[29] However, it is reported that the sacrificial agents (*i.e.*, alcohol) used in the photocatalytic synthesis of NH_3 systems can be oxidized to carbonyl compounds, which will disturb NH_3 detection in Nessler's reagent detection, thus yielding misleading results. Fig. 2a shows photographs of a solution containing Nessler's reagent and different concentrations of NH_3 solutions (0, 1.2, and 4 mg L^{-1}).[29] It can be seen that the solution color is turning from light yellow to brown with the increase in the concentration of NH_3. When 4 μg L^{-1} of formaldehyde is added, all the above solutions change into brown, indicating that trace formaldehyde can cause a remarkable color change (Fig. 2b). Therefore, the method of Nessler's reagent is not able to detect NH_3 production in the presence of this or similar sacrificial agents. In contrast, the generated carbonyl compounds have no effect on the testing method of ion chromatography (Fig. 2c and d). It is strongly recommended that the colorimetric assay methods have to be accompanied by other methods such as ion chromatography, ^{15}N isotope labeling, and *in situ* infrared spectroscopic measurements, to avoid such misleading results. Fig. 2e shows the photocatalytic performance of NH_3 synthesis *via* ion chromatography and the indophenol test.[30] The UV-vis spectra of the reaction solution containing NH_3 exhibit a maximum absorption at 630 nm (inset in Fig. 2e), which is ascribed to the indophenols. The production of NH_3 measured by ion chromatography increases with the reaction time (Fig. 2e), consistent with the results obtained by the indophenol test, indicating that indophenol is to some extent reliable.

Extensive studies on the determination of NH_3 have revealed that the indophenol blue method, Nessler's reagent method, and the ion chromatography method are accurate when the concentration of NH_3 is less than 500 μg L^{-1}, but the indophenol blue method tends to be less accurate at higher concentrations or under acidic conditions. Besides, the presence of carbonyl compounds from scavengers will enhance light adsorption in Nessler's reagent method, thus leading to an interfered detection of NH_3. Thus, to guarantee accuracy and reliability of NH_3 quantification, at least two detection methods such as the ion chromatography method and Nessler's reagent method are recommended. Furthermore, because of trace NH_3 in the ambient atmosphere, it is necessary to test the isotopically labeled $^{15}N_2$ to confirm the source of nitrogen in the product.

Open Access Article. Published on 03 11 2020. Downloaded on 2025-03-11 5:25:41.
This article is licensed under a Creative Commons Attribution 3.0 Unported Licence.

Strategies to improve photocatalytic efficiency

As mentioned above there are a few reviews summarizing the activity of diverse photocatalysts.[6,13,18,19,22] This critical review will not overlap with these reviews, but will only concentrate on the efficient strategies to improve (i) N_2 adsorption and (ii) charge separation. Such strategies include surface engineering and interface engineering for NH_3 synthesis. The photocatalytic process of NH_3 production generally includes four steps, photogeneration of charge carriers followed by their migration to the active sites, N_2 chemisorption, surface photo-oxidation and photo-reduction, and the desorption NH_3 from photocatalysts. Following the above key steps, photocatalysts can be engineered to greatly promote their catalytic activities toward NH_3 synthesis. As steps (ii), (iii) and (iv) all take place on the surface, through the study of surface regulations and interface modulations on the photocatalysts, their photocatalytic performance can be maneuvered. The surface regulations, including defect engineering and morphology engineering, significantly determine the photocatalytic activity because they can promote the surface adsorption and activation of N_2.[23,31–40,54–57,64–71] The interface modulations, including modification with cocatalysts and semiconductors, greatly affect the charge transfer and separation efficiency.[89–101,109–111] We will discuss these factors one by one below. In order to provide an intuitively systematic comparison of photocatalytic N_2 reduction systems, we list photocatalysts, reactants, NH_3 production rate, in particular the apparent quantum efficiency and detection method as shown in Table 1.

Surface regulations

Defect engineering. It is widely reported that vacancies in a photocatalyst can improve N_2 adsorption, to some extent even charge separation. There are different populations of vacancies, including oxygen vacancies, nitrogen vacancies, carbon vacancies, as well as sulfur vacancies.

Oxygen vacancies. The introduction of oxygen vacancies (OVs) can effectively facilitate N_2 adsorption and activation, as well as induce the generation of mid-gap states to promote the separation of photogenerated charge carriers.[31–42] For instance, Zhang *et al.* reported that BiOBr nanosheets with OVs on the exposed {001} facets (BOB-001-OV) could stretch the N≡N bonds from 1.078 Å to 1.133 Å, which gave strong evidence for N_2 activation over the OVs.[31] Theoretical calculations showed that the OV induced defect states could serve as the electron acceptor (Fig. 3a) to effectively suppress the recombination of electrons/holes and enhance the charge transfer from BOB-001-OV to the N_2 molecule. Fluorescence spectroscopy showed that the average lifetime (τ) of BOB-001-OV was 2.15 ns, around two times higher than that of BiOBr without OVs (BOB-001-H, Fig. 3b), proving that the OVs could promote the migration of charge carriers. With the function of OVs, BOB-001-OV showed a NH_3 yield rate of 104.3 μmol g^{-1} h^{-1} under visible light illumination in the absence of organic scavengers and noble-metal cocatalysts (Fig. 3c), and an apparent quantum efficiency (AQE) of 0.23% at 420 nm. Meanwhile, the amount of generated O_2 was stoichiometrically approaching 3/4 of the produced NH_3, which proved that water could act as an electron donor to achieve a complete chemical cycle in NH_3 photosynthesis.

Apart from the research on bismuth oxyhalide materials, Shiraishi's group utilized a series of commercial TiO_2 to study the effect of OVs on the photoreduction of N_2 to NH_3.[32] A commercial TiO_2 of JRC-TIO-6 showed an excellent performance with a steadily increasing NH_3 production within 100 h under UV light irradiation in pure water. They proposed that the Ti^{3+} species formed at the OVs on the surface of TiO_2 served as active sites, which could effectively trap the electrons and promote N_2 dissociation, resulting in a photocatalytic NH_3 production rate of 2.5 μmol h^{-1}.

In order to create the OVs, most studies used oxygen-containing catalysts. In recent years, layered double hydroxide (LDH, Fig. 4a) materials have attracted substantial attention due to their tunable electron structure and low cost.[34] Zhang's group firstly used the CuCr-LDH nanosheets (CuCr-NS) with OVs as efficient photocatalysts for NH_3 photosynthesis.[34] The OVs over CuCr-NS surface were created by the reduction of thickness and the in-plane compressive strain (Fig. 4b). The optimal CuCr-NS exhibited a NH_3 production rate of 78.6 μmol g^{-1} h^{-1} under full-spectrum irradiation (Fig. 4c), and an AQE of 2.4% at 400 nm. Subsequently, they further reported another work on ZnAl-LDH nanosheets for optimal OVs by incorporating coordinately unsaturated $Cu^{\delta+}$ species.[35] The DFT calculations implied that the OVs and $Cu^{\delta+}$ species in ZnAl-LDH could effectively promote N_2 adsorption and activation, leading to a remarkable NH_3 yield of 110 μmol L^{-1} h^{-1} in pure water under UV-vis irradiation. Therefore, the creation of OVs on the surface of photocatalysts paves a way for developing other innovative materials toward photocatalytic N_2 reduction.

Nitrogen vacancies/carbon vacancies. Inspired by the conclusion of N_2 activation and efficient electron transfer by OVs on the catalyst surface, nitrogen vacancies (NVs) were later studied for the NRR process. Because of its excellent optical properties, low cost, and good stability, graphitic carbon nitride (g-C_3N_4) has attracted much scientific interest in the field of photocatalysis.[42–53] Dong *et al.* have reported the application of NV-incorporated g-C_3N_4 (V-g-C_3N_4) for N_2 photoreduction.[54] They found that the N_2 adsorption amount of V-g-C_3N_4 was 75.1 cm^3 g^{-1}, 2.4 times higher than that of g-C_3N_4 without NVs (30.9 cm^3 g^{-1}), which suggested that the NVs on the surface of V-g-C_3N_4 could provide a number of chemisorption and activation sites for N_2 molecules, leading to an NH_3 production rate of 1.24 mmol h^{-1} g_{cat}^{-1} under visible light irradiation in the presence of methanol as a hole scavenger. Recently, a g-C_3N_4 catalyst modified with cyano groups (–C≡N) and intercalated K^+ (mCNN) was prepared as an efficient photocatalyst for NRR.[55] Relative to pristine g-C_3N_4, the absorption spectrum of mCNN was extended to the whole visible region (Fig. 5a), resulting from the π–π* electronic transitions in the conjugated heterocyclic rings and the n–π* electronic transitions at the

© 2021 The Author(s). Published by the Royal Society of Chemistry

Open Access Article. Published on 03 11 2020. Downloaded on 2025-03-11 5:25:41.
This article is licensed under a Creative Commons Attribution 3.0 Unported Licence.

Table 1 Photocatalytic performance of different catalysts for NH_3 synthesis

Catalyst	Reaction medium	Scavenger	Light source	Ammonia yield	Apparent quantum efficiency (AQE)	Ammonia detection method	Ref.
BiOBr-001-OV	N_2/H_2O (l)	None	$\lambda > 420$ nm	104.3 μmol g^{-1} h^{-1}	0.23% at 420 nm	Nessler's reagent	31
JRC-TIO-6	N_2/H_2O (l)	2-PrOH	$\lambda > 280$ nm	2.5 μmol g^{-1} h^{-1}	Not reported	Indophenol blue method	32
CuCr-LDH	N_2/H_2O (l)	None	Full spectrum	78.6 μmol g^{-1} h^{-1}	2.4% at 400 nm	Nessler's reagent	34
ZnAl-LDH	N_2/H_2O (l)	None	UV-vis	110 μmol L^{-1} h^{-1}	1.77% at 265 nm, 0.56% at 365 nm	Ion chromatography	35
V-g-C_3N_4	N_2/H_2O (l)	Methanol	$\lambda > 420$ nm	1.24 mmol h^{-1} g_{cat}^{-1}	Not reported	Nessler's reagent	54
mCNN	N_2/ethylene glycol (l)	Ethylene glycol	$\lambda > 400$ nm	3.42 mmol g^{-1} h^{-1}	Not reported	Nessler's reagent	55
SCNNSs	N_2/H_2O (l)	Methanol	Full spectrum	5.99 mmol h^{-1} g_{cat}^{-1}	Not reported	Nessler's reagent	56
$Mo_{0.1}Ni_{0.1}Cd_{0.8}S$	N_2/H_2O (l)	Ethanol	UV	3.2 mg h^{-1} g_{cat}^{-1}	Not reported	Nessler's reagent	57
0.2 wt% Fe-doped TiO_2	N_2/H_2O (g)	None	UV	11.6 μmol g^{-1} h^{-1}	Not reported	Indophenol blue method	17
0.4 wt% Co-doped TiO_2	N_2/H_2O (l)	None	UV	6.3 μmol g^{-1} h^{-1}	Not reported	Indophenol blue method	17
0.4 wt% Cr-doped TiO_2	N_2/H_2O (l)	None	UV	0.37 μmol g^{-1} h^{-1}	Not reported	Indophenol blue method	17
0.4 wt% Mo-doped TiO_2	N_2/H_2O (l)	None	UV	6.7 μmol g^{-1} h^{-1}	Not reported	Indophenol blue method	17
Fe-Doped TiO_2	N_2/H_2O (l)	Ethanol	$\lambda = 254$ nm	1.2 mmol L^{-1}	Not reported	Nessler's reagent	64
Fe-Doped $SrMoO_4$	N_2/H_2O (l)	None	UV-vis	93.1 μmol g^{-1} h^{-1}	Not reported	Nessler's reagent, indophenol blue method	65
Fe-Doped BiOCl	N_2/H_2O (l)	None	Full spectrum	1.022 mmol g^{-1} h^{-1}	1.8% at 420 nm	Indophenol blue method	66
Mo-Doped $W_{18}O_{49}$	N_2/H_2O (l)	Na_2SO_3	Full spectrum	195.5 μmol g^{-1} h^{-1}	0.33% at 400 nm	Nessler's reagent, ion chromatography	67
Cu-Doped TiO_2	N_2/H_2O (l)	None	Full spectrum	78.9 μmol g^{-1} h^{-1}	0.08% at 600 nm, 0.05% at 700 nm	Nessler's reagent, ion chromatography	68
FePt@C_3N_4	N_2/H_2	None	$\lambda > 400$ nm	63 μg h^{-1} g^{-1}	0.15% between 450 and 500 nm	Colorimetric method, ion chromatography	72
B-Doped g-C_3N_4	N_2/H_2O (l)	Na_2SO_3	$\lambda > 400$ nm	313.9 μmol g^{-1} h^{-1}	0.64% at 420 nm	Nessler's reagent	73
C-Doped TiO_2	N_2/H_2O (l)	Methanol	$\lambda > 420$ nm	109.3 μmol g^{-1} h^{-1}	2.4% at 400 nm	Ion chromatography	
Bi_5O_7I-001	N_2/H_2O (l)	Methanol	280–800 nm	111.5 μmol g^{-1} h^{-1}	5.1% at 365 nm	Nessler's reagent	77
BiOCl-010	N_2/H_2O (l)	Methanol	Full spectrum	92.4 μmol g^{-1} h^{-1}	4.3% at 254 nm	Nessler's reagent	78
BiO	N_2/H_2O (l)	None	Full spectrum	1226 μmol g^{-1} h^{-1}	Not reported	Indophenol blue method	86
Bi_5O_7Br-NT	N_2/H_2O (l)	None	$\lambda > 400$ nm	1.38 mmol g^{-1} h^{-1}	2.3% at 420 nm	Nessler's reagent	87
eBP NFs	N_2/H_2O (l)	Na_2SO_3, $Na_2S\cdot 9H_2O$	$\lambda = 420$ nm	2.37 mmol g^{-1} h^{-1}	Not reported	Nessler's reagent	88
SiO_2/C-RP	N_2/H_2O (l)	None	Full spectrum	0.73 μmol h^{-1}	Not reported	Ion chromatography	89
Ru-Loaded TiO_2	N_2/H_2O (l)	Methanol	Full spectrum	29.4 μmol g^{-1} h^{-1}	Not reported	Indophenol blue method	93
Ru-Loaded TiO_2	N_2/H_2O (l)	Ethanol	Full spectrum	56.3 μg h^{-1} g_{cat}^{-1}	Not reported	Indophenol blue method	95
Au/TiO_2-OV	N_2/H_2O (l)	Methanol	$\lambda > 420$ nm	78.6 μmol g^{-1} h^{-1}	0.82% at 550 nm	Indophenol blue method	96
Ti_3C_2-P25	N_2/H_2O (l)	None	Full spectrum	10.74 μmol g^{-1}	Not reported	Ion chromatography	103
Pt-Loaded ZnO	N_2/H_2O (l)	Na_2SO_3	UV	860 mmol g^{-1} h^{-1}	Not reported	Indophenol blue method	104
SV-1T-MoS_2/CdS	N_2/H_2O (l)	Methanol	420–780 nm	8220.83 μmol L^{-1} h^{-1} g^{-1}	4.424% under simulated solar light	Nessler's reagent	105
NiS/CdS	N_2/H_2O (l)	None	Full spectrum	2.8 mg L^{-1} h^{-1}	0.76% at 420 nm	Nessler's reagent	106
Pt-SACs/CTF	N_2/H_2O (l)	None	420–780 nm	171.4 μmol g^{-1} h^{-1}	1.4% at 420 nm	Nessler's reagent	107
Ru/RuO_2/g-C_3N_4	N_2/H_2O (l)	Methanol	Full spectrum	13.3 μmol g^{-1} h^{-1}	Not reported	Ion chromatography	108
Fe@graphene	N_2/H_2, 200 °C	None	200–600 nm	420 μg g_{cat}^{-1} h^{-1}	Not reported	Indophenol blue method	110
g-C_3N_4/Bi_2MoO_6	N_2/H_2O (l)	Methanol	$\lambda > 420$ nm	3271 μmol L^{-1} g^{-1}	Not reported	Nessler's reagent	111
TiO_2@C/g-C_3N_4	N_2/H_2O (l)	Methanol	$\lambda > 420$ nm	250.6 μmol g^{-1} h^{-1}	0.14% at 420 nm	Nessler's reagent	112
Bi_2MoO_6/OV-BiOBr	N_2/H_2O (l)	None	Full spectrum	81.0 μmol g^{-1} h^{-1}	Not reported	Nessler's reagent	116

active N defect sites (–C≡N), which indicated that the introduction of the N-defect of –C≡N could significantly change the optical properties. Fig. 5b displays the band structures of mCNN and pristine g-C_3N_4 through the results of experiments.

Open Access Article. Published on 03 11 2020. Downloaded on 2025-03-11 5:25:41.
This article is licensed under a Creative Commons Attribution 3.0 Unported Licence.

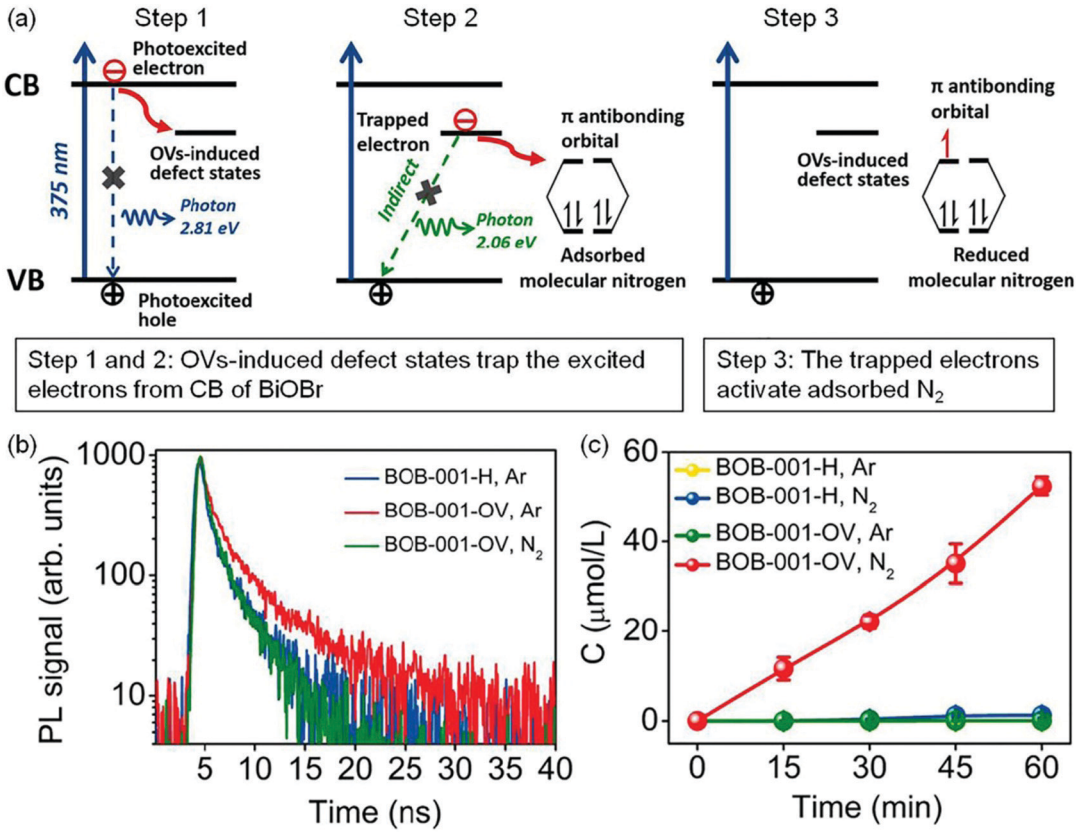

Fig. 3 Schematic of the OV-induced enhanced interfacial electron transfer processes over BOB-001-OV. (b) Time-resolved photoluminescence (PL) spectra of BOB-001-OV and BOB-001-H. (c) The photocatalytic NH_3 production of BOB-001-OV and BOB-001-H under visible light ($\lambda > 420$ nm). Reproduced from ref. 31 with permission from ACS Publication.

Compared with pristine g-C_3N_4, a subgap state was presented for mCNN, which could be ascribed to the N defect, resulting in a broad visible-light response. The enhanced EPR intensity (Fig. 5c) of mCNN compared to pristine g-C_3N_4 was assigned to the strong electron withdrawing groups of –C≡N on mCNN, which could delocalize the isolated electrons in mCNN, therefore promoting the separation of photocarriers and increasing the generation of active radical species to boost the activity of NH_3 photosynthesis. The rate of NH_3 generation of the mCNN photocatalyst was measured to be 3.42 mmol g^{-1} h^{-1} with ethylene glycol as a scavenger under visible light irradiation (Fig. 5d), which was much higher than that of pristine g-C_3N_4 (1.11 mmol g^{-1} h^{-1}). The DFT calculations revealed that K^+ could be linked to the unsaturated C centers by coordination as shown in Fig. 5e, which could adsorb N_2 as the lone-pair electrons of nitrogen would fill the empty state in K^+ (ΔG = −0.28 eV), followed by the rearrangement of K^+ with the C atom and the adsorption of N_2 (ΔG = −0.17 eV). Because of the large ion hydration free energy of K^+, it could be extracted back into solution, then forming a C_2N_4 ring (ΔG = 1.64 eV) intermediate which could undergo a MvK process to regenerate –C≡N, thereby stabilizing the unsaturated C sites.

Apart from the above NVs on the g-C_3N_4 photocatalyst, carbon vacancies (CVs) on a porous sulfur-doped g-C_3N_4 (SCNNSs) have also been exploited.[56] The introduction of CVs was proved to play the same role as NVs, while the S-doping effect was demonstrated to improve the separation efficiency of photogenerated electron–hole pairs. Taking these advantages, the optimal SCNNSs showed an NH_3 production rate of 5.99 mmol h^{-1} $g_{cat}{}^{-1}$.

Sulfur vacancies. Considering the importance of the sulfur element in nitrogenases, a few have reported the effects of sulfur vacancies (SVs) on N_2 photoreduction. It was reported that SVs could be created on the surface of $Mo_{0.1}Ni_{0.1}Cd_{0.8}S$ by co-doping Mo and Ni into CdS.[57] N_2-temperature-programmed desorption (N_2-TPD) results illustrated that the SVs on the surface of $Mo_{0.1}Ni_{0.1}Cd_{0.8}S$ obviously enhanced N_2 chemisorption (Fig. 6a), which was beneficial for NRR. Importantly, the photocatalytic NH_3 generation rate of $Mo_{0.1}Ni_{0.1}Cd_{0.8}S$ was linearly related to its SV concentration as shown in Fig. 6b. As the concentration of SVs increased, there was an increase in the photocatalytic NH_3 production rate. This result suggested that the SVs played a vital role in the photoreduction of N_2. The $Mo_{0.1}Ni_{0.1}Cd_{0.8}S$ with the highest SV concentration showed the highest NH_3 production rate of 3.2 mg h^{-1} $g_{cat}{}^{-1}$ (Fig. 6b).

Doping. Metal doping is a very promising strategy to change the electronic structure and surface property of photocatalysts to enhance the photocatalytic activity.[58–63] In one report,

© 2021 The Author(s). Published by the Royal Society of Chemistry

Open Access Article. Published on 03 11 2020. Downloaded on 2025-03-11 5:25:41.
This article is licensed under a Creative Commons Attribution 3.0 Unported Licence.

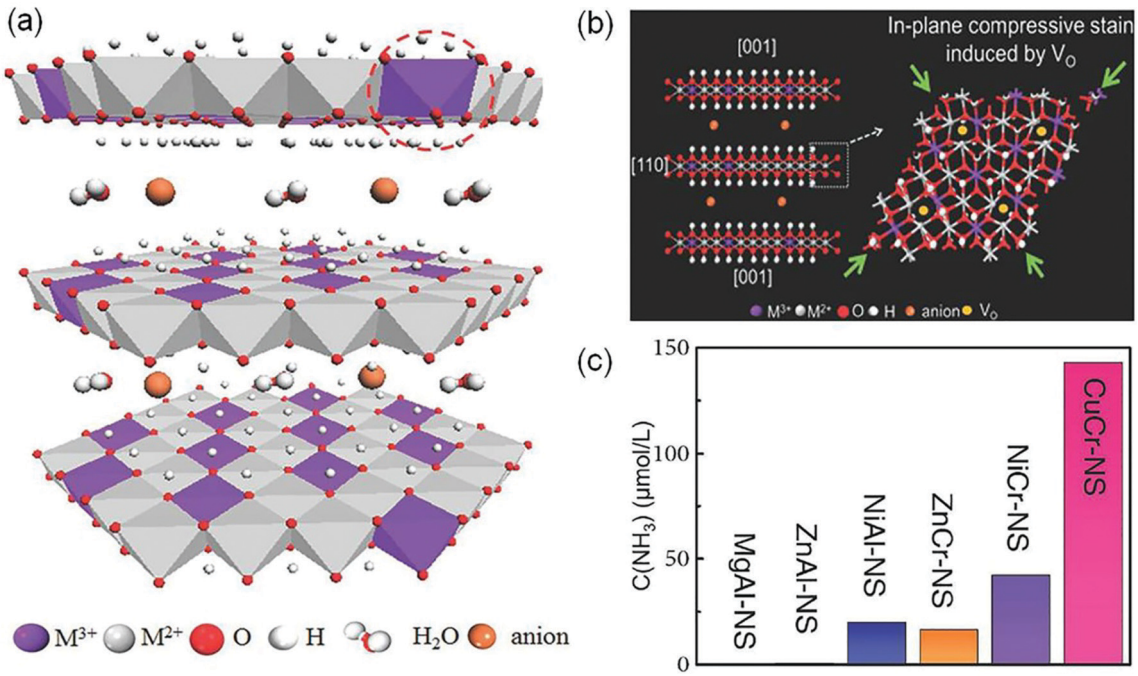

Fig. 4 (a) Schematic representation of the layered LDH structure with defective MO_6 octahedra. (b) Schematic of the in-plane biaxial compressive strain in CuCr-NS. (c) The yield of NH_3 over different LDH photocatalysts under visible-light illumination ($\lambda > 400$ nm). Reproduced from ref. 34 with permission from Wiley-VCH.

Schrauzer *et al.* studied the effect of different metal doped TiO_2 on the photocatalytic activity of N_2 reduction, including iron (Fe), chromium (Cr), cobalt (Co), and molybdenum (Mo).[17] They found that Fe doping was the most effective for enhancing the photocatalytic activity of TiO_2 for photosynthesis of NH_3 from N_2 and H_2O. However, O_2 production as the oxidation product was not reported. In this regard, Zhao *et al.* investigated the Fe-doped TiO_2 with highly exposed (101) facets for N_2 photofixation,[64] and found that an optimum Fe^{3+} doping content played a key role in inhibiting the recombination of photoinduced electron–hole pairs, which could act as a temporary electron/hole trapping sites, therefore enhancing the concentration of charge carriers and improving the photocatalytic performance. With this in mind, Liu *et al.* also reported a Fe-doped $SrMoO_4$ (FSMO) as a potential candidate for N_2 photoreduction.[65] Further studies revealed that the intrinsic bandgap of $SrMoO_4$ could be shrunk from 3.98 eV to 2.93 eV with the increase in Fe doping concentration (from 0 to 5.1%), resulting in the extension of light adsorption from the ultraviolet to the visible-light region. Besides that, the Fe doping could induce the formation of surface defects as active sites for N_2 adsorption and significantly retard the recombination of electrons and holes, leading to enhanced N_2 reduction reaction. As a result of these properties, an improved NH_3 production rate of 93.1 μmol g^{-1} h^{-1} over the optimal FSMO was achieved compared with that of pristine $SrMoO_4$ (66.7 μmol g^{-1} h^{-1}). In another related work incorporating Fe into BiOCl nanosheets, Fe-doped BiOCl nanosheets (BiOCl NSs-Fe) were developed for N_2 photoreduction.[66] The optimal BiOCl NSs-Fe exhibited a marked enhancement of photocatalytic NH_3 production, and the efficiency was 2.53 times higher than that of pristine BiOCl NSs.

In another study, Mo was successfully doped into $W_{18}O_{49}$ nanowires to produce Mo-doped $W_{18}O_{49}$ nanowires (MWO-1) as shown in Fig. 7a.[67] Compared with OV-rich $W_{18}O_{49}$ nanowires, Mo-doping had many kinds of effects on photocatalytic N_2 reduction. Fig. 7b displays the electronic band structures of MWO-1 and $W_{18}O_{49}$; it is observed that the defect-band center could be shifted to the Fermi level by Mo doping, which provided more energetic electrons for NRR. Theoretical simulations revealed that the Mo–W centers could alter electron distribution, leading to a larger adsorption energy (−2.48 eV) relative to $W_{18}O_{49}$ with W–W sites (1.65 eV), which was in favor of N_2 chemisorption and activation (Fig. 7c). Additionally, the enhanced M–O co-valence caused by Mo doping could effectively promote the electron transfer from metal active centers to adsorbed N_2 molecules. Thus, the optimal MWO-1 exhibited an excellent NH_3 yield rate of 195.5 μmol g^{-1} h^{-1} under full-spectrum irradiation (Fig. 7d), which was 7 times higher than that of $W_{18}O_{49}$, and also realized a high AQE of 0.33% at 400 nm.

Furthermore, Cu-doped ultrathin TiO_2 nanosheets (TiO_2-V_O-strain) were also studied.[68] Compared with pristine TiO_2, introducing Cu into TiO_2 could create abundant OVs and cause lattice distortion and strain effects, resulting in a significant increase of N_2 adsorption energy on the surface of TiO_2-V_O-strain (−0.37 eV) compared with that of pristine TiO_2 (−0.17 eV, Fig. 8a). The increased adsorption energy promoted the electron transfer from TiO_2 to N_2, thereby breaking the N≡N bonds. Meanwhile, the required reaction energy for N_2 hydrogenation to

Open Access Article. Published on 03 11 2020. Downloaded on 2025-03-11 5:25:41.
This article is licensed under a Creative Commons Attribution 3.0 Unported Licence.

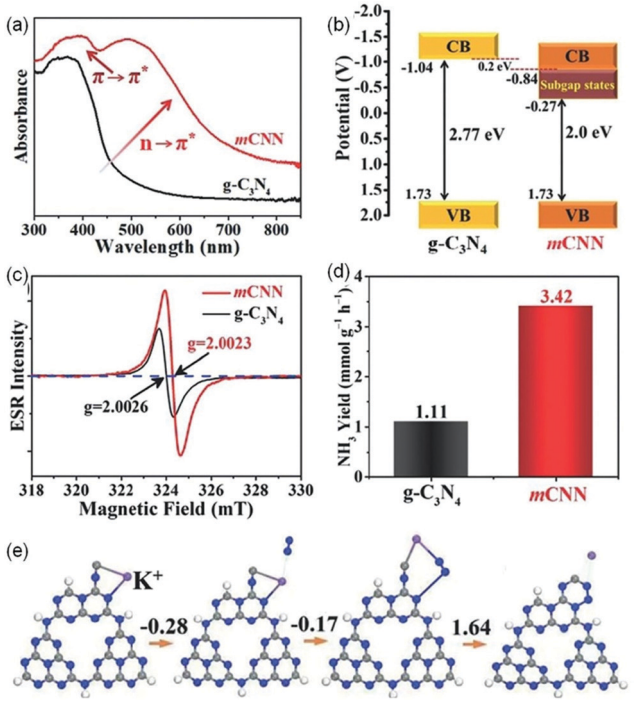

Fig. 5 (a) UV-vis diffuse reflectance spectra (DRS). (b) Schematic illustration of energy band structures. (c) Room-temperature electron paramagnetic resonance (EPR) spectra. (d) NH_3 production rates of g-C_3N_4 and mCNN. (e) The calculated free-energy changes for the NRR pathway using mCNN. The blue sphere represents N, the grey sphere represents C, the white sphere represents H, and the purple sphere represents K^+. Reproduced from ref. 55 with permission from Wiley-VCH.

N–NH* was only 0.365 eV on TiO_2-V_o-strain, which was lower than that on pristine TiO_2 (2.115 eV, Fig. 8b). As a result, the optimal TiO_2-V_o-strain (6% TiO_2) achieved an enhanced NH_3 yield rate of 78.9 μmol g^{-1} h^{-1} under full solar irradiation, about 5.2 times higher than that of the TiO_2 nanosheets with OVs (0% TiO_2, Fig. 8c). In addition, the yield rate of O_2 (59.1 μmol g^{-1} h^{-1}) and NH_3 mentioned above over TiO_2-V_o-strain was close to the stoichiometric ratio of 3 : 4, revealing that the protons in NH_3 were from the H_2O molecules. Most recently, a novel bimetallic system with Fe–Pt loaded g-C_3N_4 was used for efficient ammonia synthesis under mild conditions.[72] Further investigations proposed that the doping of Pt onto the Fe nanocluster over the surface of g-C_3N_4 could cause an uplift of the energy band of semiconductors and form a large Schottky barrier, thus leading to an improved separation of photogenerated carriers and enhanced N_2 reduction. Accordingly, 0.3 wt% Pt doped on 3 wt% Fe@C_3N_4 exhibited a high NH_3 production rate of 63 μg h^{-1} g^{-1} with gaseous H_2 and N_2 as reactants under visible light irradiation and the AQE was tested to be 0.15% between 450 and 500 nm.

Apart from metal doping, a metal-free B-doped g-C_3N_4 nanosheet (BCN) with exposed active N atoms was recently synthesized for highly efficient ammonia synthesis.[73] Theoretical studies revealed that the exposed N atoms could be stabilized by B–N–C coordination on BCN, which was different from that in the pristine g-C_3N_4. The B dopants were proved as active sites for N_2 adsorption and activation and could effectively retard charge recombination and improve light utilization. The optimal BCN with 13.8 wt% B-dopants exhibited a remarkable NH_3 yield rate of 313.9 μmol g^{-1} h^{-1} under visible light irradiation in the presence of Na_2SO_3 as a hole scavenger, which was much higher than that (32.8 μmol g^{-1} h^{-1}) over pristine g-C_3N_4 and also achieved a good QE of around 0.64% at 420 nm. In addition, carbon-doped TiO_2 was also reported for N_2 photoreduction, which exhibited an NH_3 yield rate of 109.3 μmol g^{-1} h^{-1}.

Morphology engineering

Facets. Since the surface atomic distribution has a huge effect on the active sites and electronic structures of photocatalysts,[69,74–76] many researchers attempted to control the crystal facet of semiconductors to enhance the photocatalytic N_2 reduction. For instance, two Bi_5O_7I nanosheets with different {100} and {001} facets were synthesized successfully *via* hydrolysis and calcination methods, respectively.[77] Further investigations

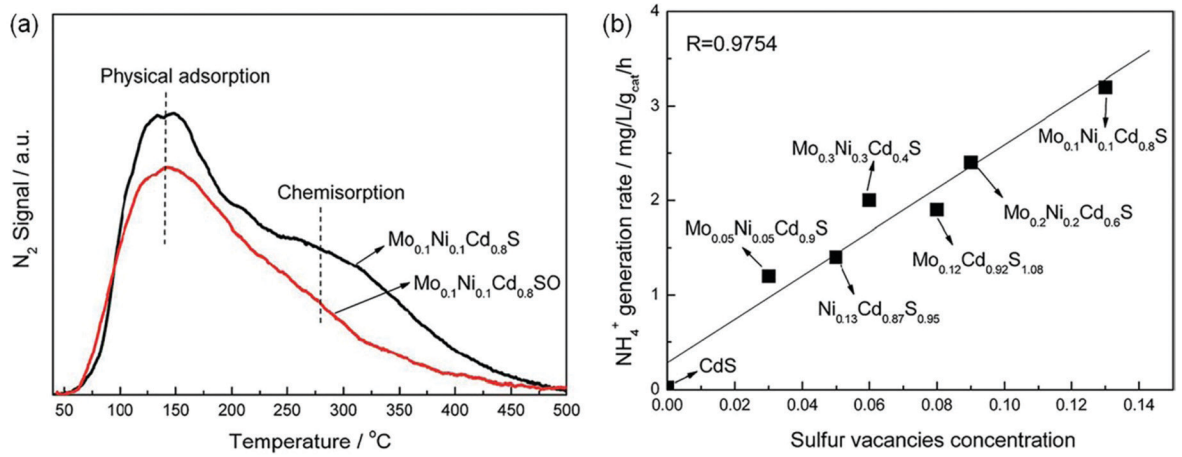

Fig. 6 (a) The N_2-TPD of $Mo_{0.1}Ni_{0.1}Cd_{0.8}S$ and $Mo_{0.1}Ni_{0.1}Cd_{0.8}S$. (b) The relationship of NH_3 yield over the obtained photocatalysts and the SV concentration. Reproduced from ref. 57 with permission from The Royal Society of Chemistry.

© 2021 The Author(s). Published by the Royal Society of Chemistry

Open Access Article. Published on 03 11 2020. Downloaded on 2025-03-11 5:25:41.
This article is licensed under a Creative Commons Attribution 3.0 Unported Licence.

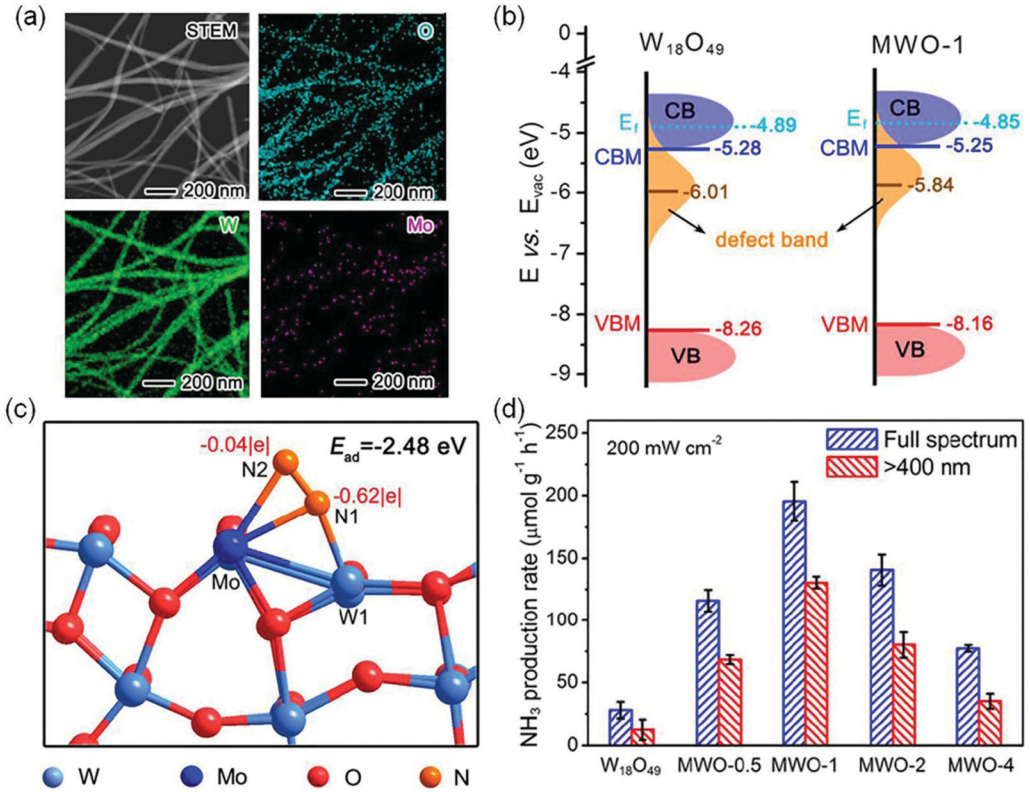

Fig. 7 (a) The scanning TEM (STEM) image and the corresponding elemental mapping of MWO-1. (b) Schematic illustration of the band structures of $W_{18}O_{49}$ and MWO-1. (c) Schematic simulation for N_2 adsorption and activation on the surface active sites of the Mo-doped $W_{18}O_{49}$ model. (d) The photocatalytic NH_3 yield on various catalysts. Reproduced from ref. 67 with permission from ACS Publication.

revealed that Bi_5O_7I-001 had more negative conduction band position (−1.45 eV) compared with that in Bi_5O_7I-100 (−0.85 eV) and exhibited higher efficiency for separation of photoinduced carriers, thus leading to a high photocatalytic activity for N_2 photoreduction. Accordingly, a remarkable NH_3 generation rate of 111.5 μmol g^{-1} h^{-1} over Bi_5O_7I-001 was achieved using methanol as a hole scavenger and the AQE of that was increased to 5.1%.

In another report, Zhang *et al.* also systematically investigated the influence of {001} and {010} facets of OV-rich BiOCl nanosheets on N_2 adsorption and activation.[78] Experimental results showed that {010} facet BiOCl nanosheets (BOC-010) exhibited a superior performance with a NH_3 yield of 4.62 μmol g^{-1} h^{-1}, which was around 2.5 times higher than that on {001} facet BiOCl nanosheets (BOC-001, Fig. 9a). Meanwhile, it was observed that N_2H_4 which served as a main intermediate was accumulated on BOC-010 during N_2 photoreduction reaction within 30 min and was consumed gradually to be converted into NH_3 (Fig. 9b). Importantly, when N_2H_4 was used as the reactant, both BOC-010 and BOC-001 showed a similar photocatalytic conversion efficiency of N_2H_4 under simulated solar irradiation (Fig. 9c), which in turn meant that BOC-010 had a stronger ability to generate N_2H_4 intermediates. Further DFT calculations revealed that the N_2 fixation on BOC-010 followed an alternative pathway with N_2H_4 as the main intermediate, which could provide a lower energy pathway for N_2 fixation *via* proton-coupled electron transfer compared with that *via* a distal pathway occurring on BOC-001 facets, thus resulting in enhanced NH_3 production (Fig. 9d and e).

Nanostructure engineering. Nanomaterials have preternatural interface structures and unique functions, such as the small size effect, the surface and boundary effect, quantum size and so on.[79–85] In order to increase the catalytic active sites of the photocatalytic reduction of N_2, Sun *et al.* synthesized BiO quantum dots with an average size of 2–5 nm (Fig. 10a), which showed an NH_3 production rate of 1226 μmol g^{-1} h^{-1} without a cocatalyst and a sacrificial agent.[86] Meanwhile, the amount of produced O_2 increased continuously with increasing irradiation time, consistent with the stoichiometric chemistry. Kinetic analysis and quantum chemical calculations suggested that the highly efficient photocatalytic activity of BiO quantum dots could be attributed to the fact that the smaller size endowed the surface and edge of BiO rich in Bi^{2+} species, which had the potential to increase the electron donation to the anti-bonding π* orbitals of N_2, thereby could act as active sites to adsorb and activate N_2 (Fig. 10b). More recently, a tubular OV-rich Bi_5O_7Br (Bi_5O_7Br-NT) with a diameter of 5 nm (Fig. 10c) was prepared and it exhibited a maximum NH_3 yield rate of 1.38 mmol g^{-1} h^{-1} (Fig. 10d) upon changing the OV concentration.[87] A high specific surface area of up to 96.56 m^2 g^{-1} was observed for Bi_5O_7Br-NT, which indicated the exposure of abundant surface

Open Access Article. Published on 03 11 2020. Downloaded on 2025-03-11 5:25:41.
This article is licensed under a Creative Commons Attribution 3.0 Unported Licence.

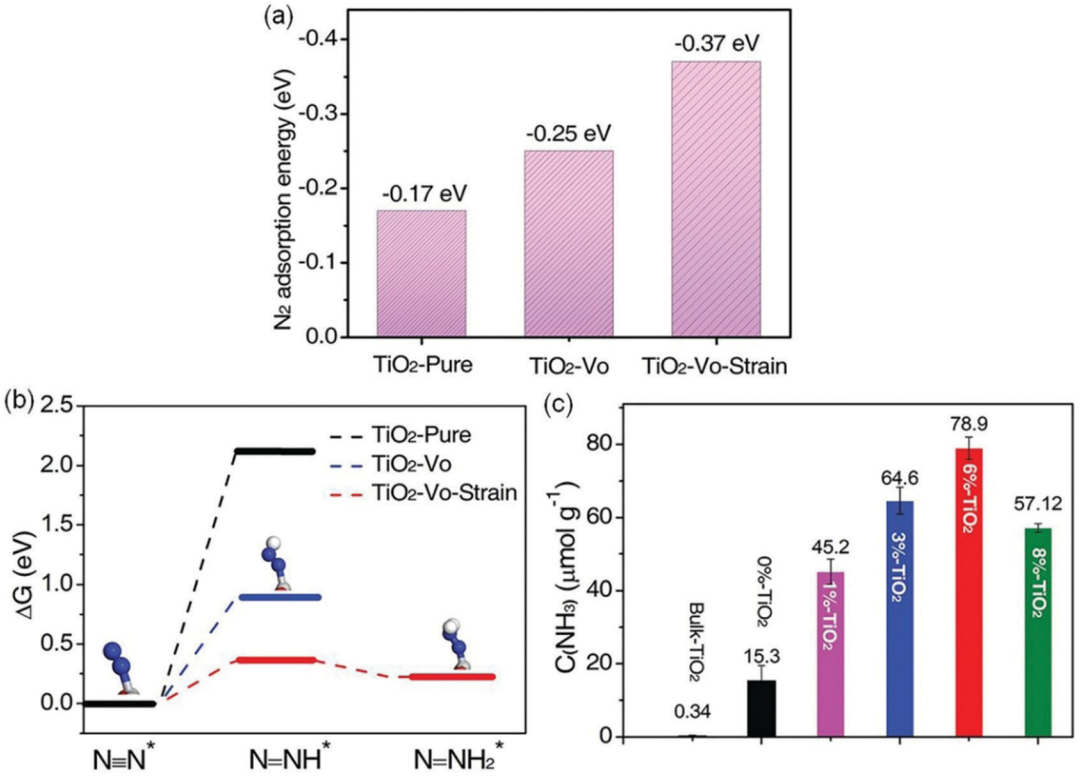

Fig. 8 (a) The N_2 adsorption energies by DFT calculations on different photocatalysts. (b) The calculated Gibbs free energy for N_2 reduction on the (001) surface of different photocatalysts (H: white sphere, Ti: gray sphere, N: blue sphere, O: red sphere). (c) Yield of NH_3 over various samples under UV-vis irradiation. Reproduced from ref. 68 with permission from Wiley-VCH.

OVs for the chemisorption and activation of N_2. It was found that the OVs on the Bi_5O_7Br-NT surface could not only effectively promote N_2 adsorption and activation, but also could be regenerated by capturing O atoms from H_2O after the reaction to maintain the good stability of Bi_5O_7Br nanostructures. As a result, the calculated AQE for the Bi_5O_7Br-NT photocatalyst was 2.3% under visible light irradiation at 420 nm (Fig. 10e). Furthermore, it was reported that metal-free black phosphorus nanoflakes with abundant edges (eBP NFs) synthesized *via* a facile chemical etching exfoliation method exhibited a remarkable NH_3 yield rate of 2.37 mmol g^{-1} h^{-1} under visible light irradiation in the presence of Na_2SO_3 and $Na_2S{\cdot}9H_2O$ as scavengers.[88] The photoelectrochemical characteristics (PEC) and transient absorption (TA) studies revealed that the efficient ammonia synthesis was attributed to rich edges on the surface, which could provide abundant active sites for enhanced N_2 adsorption and activation. Similarly, a nanocomposite (SiO_2/C-RP) prepared by loading red phosphorus on SiO_2 nanospheres showed superior charge separation.[89] Besides, this hybrid nanostructure exhibited a large surface area, good water dispersibility and large light adsorption. As a result of these benefits, SiO_2/C-RP exhibited an NH_3 production yield of 0.73 μmol h^{-1} under full-spectrum irradiation.

Interfacial modulation

Cocatalyst loading. With the similar idea of using metal cocatalysts to inhibit the recombination of electrons and holes and enhance the photostability of catalysts in other photocatalytic processes, e.g. water splitting,[90–102] Ranjit *et al.* studied different metal loaded TiO_2 toward the photoreduction of N_2, including ruthenium (Ru), rhodium (Rh), palladium (Pd), and platinum (Pt).[93] It was found that the order of the photocatalytic activity of these metals on TiO_2 was Ru > Rh > Pd > Pt. The excellent performance of Ru-loaded TiO_2 could be assigned to the high metal–hydrogen bond strength which well correlated with the high production of NH_3. In recent years, single-atom catalysts (SACs) have been well studied as excellent candidates for boosting the catalytic activity and improving the utilization efficiency of metal atoms during the photocatalytic process.[94] To further improve the performance of the photocatalytic NH_3 synthesis, a single atomic Ru decorated TiO_2 nanosheet with abundant OVs was prepared.[95] The DFT calculations indicated that the single atomic Ru species were favorable to be formed and dispersed on the OVs over the TiO_2 nanosheet surface. Further investigations revealed that the isolated Ru atom could serve as the active site for N_2 adsorption and activation, promote the separation of photogenerated charge carriers efficiently, as well as inhibit the competitive H_2 evolution reaction, thus leading to an improved NH_3 photosynthesis. Thus, a 1 wt% single Ru atom decorated TiO_2 nanosheet exhibited a superior performance with an NH_3 yield of 56.3 μg h^{-1} g_{cat}^{-1}, which was two times as high as that of pure TiO_2. Recently, Au-anchored TiO_2 nanosheets with OV (Au/TiO_2-OV) photocatalysts were developed for N_2 photofixation.[96] As shown in Fig. 11a, Au nanospheres

© 2021 The Author(s). Published by the Royal Society of Chemistry

Open Access Article. Published on 03 11 2020. Downloaded on 2025-03-11 5:25:41.
This article is licensed under a Creative Commons Attribution 3.0 Unported Licence.

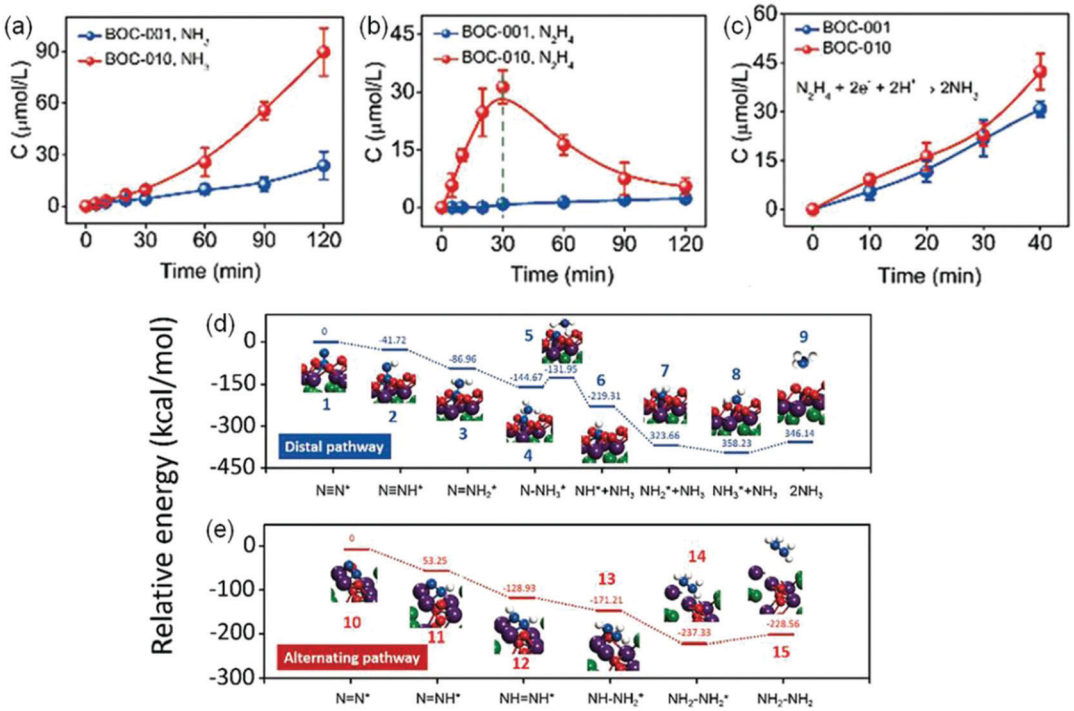

Fig. 9 Photocatalytic performance for N_2 reduction on BOC-001 and BOC-010. The yield comparison of produced (a) NH_3 and (b) N_2H_4 on BOC-001 and BOC-010 under simulated solar light irradiation. (c) The NH_3 yield produced from N_2H_4 BOC-001 and BOC-010 under simulated solar light irradiation. The calculated free energy change for N_2 reduction (d) on the (001) surface *via* a distal pathway and (e) on the (010) surface *via* an alternating pathway. Reproduced from ref. 78 with permission from The Royal Society of Chemistry.

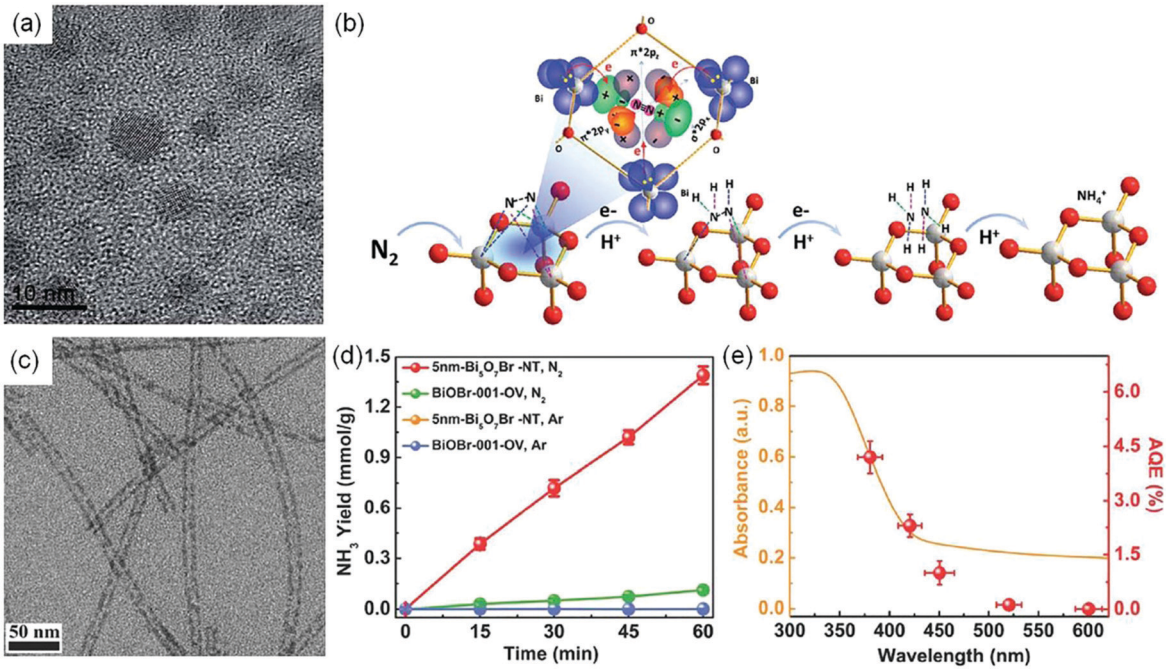

Fig. 10 (a) TEM image of BiO quantum dots. (b) Proposed mechanism for N_2 photoreduction on BiO quantum dots. Reproduced from ref. 86 with permission from The Royal Society of Chemistry. (c) TEM image of Bi_5O_7Br-NT. (d) Yield of NH_3 for Bi_5O_7Br-NT. (e) The wavelength-dependent AQE of Bi_5O_7Br-NT. Reproduced from ref. 87 with permission from Wiley-VCH.

with a diameter of 20 nm ± 1.4 nm were uniformly distributed on the surface of TiO_2-OV nanosheets. The UV-vis spectrum of Au/TiO_2-OV showed absorption characteristics of Au loaded TiO_2 (Au/TiO_2) and TiO_2-OV, displaying a broad localized

Open Access Article. Published on 03 11 2020. Downloaded on 2025-03-11 5:25:41.
This article is licensed under a Creative Commons Attribution 3.0 Unported Licence.

surface plasmon resonance (LSPR) peak at 550 nm and an obvious absorption tail (Fig. 11b). Therefore, in the Au/TiO_2-OV hybrid, OVs on the surface of TiO_2 nanosheets chemisorbed and activated N_2 molecules, which were reduced to NH_3 by plasmon-induced hot electrons from Au nanoparticles in the presence of methanol as a hole scavenger (Fig. 11c). As a result, the optimal Au/TiO_2-OV exhibited an NH_3 photoproduction rate of 78.6 μmol g^{-1} h^{-1}, which was 98 and 35 times higher than that of Au/TiO_2 and TiO_2-OV respectively (Fig. 11d). Recently, we reported a hybrid of 2D layered Ti_3C_2 and P25 TiO_2 (Ti_3C_2-P25), in which Ti_3C_2 served as the cocatalyst to facilitate charge separation due to its excellent electrical conductivity. The DFT calculation (Fig. 11e) revealed that the N_2 adsorption energies were ranked as Ti_3C_2 (2.731 eV) > VOs-TiO_2 (0.342 eV) > TiO_2 (0.170 eV), implying that Ti_3C_2 had a much stronger N_2 chemisorption effect compared with VOs-TiO_2 and TiO_2. Therefore the introduction of Ti_3C_2 on P25 could accelerate N_2 chemisorption, leading to five times higher photocatalytic yield of NH_3 than that on pure P25. More importantly, water acted as the electron donor in this study and stoichiometric O_2 production was also observed, which was one of a few examples that could observe the stoichiometric reduction and oxidation products.[103]

In addition to TiO_2-based photocatalysts, Pt-loaded ZnO was reported as an efficient photocatalyst for N_2 photoreduction which exhibited an NH_3 yield rate of 860 mmol g^{-1} h^{-1}.[104] More recently, O-doped 1T-MoS_2 nanosheets with a large amount of SVs (SV-1T-MoS_2) were used as cocatalysts over CdS nanorods for

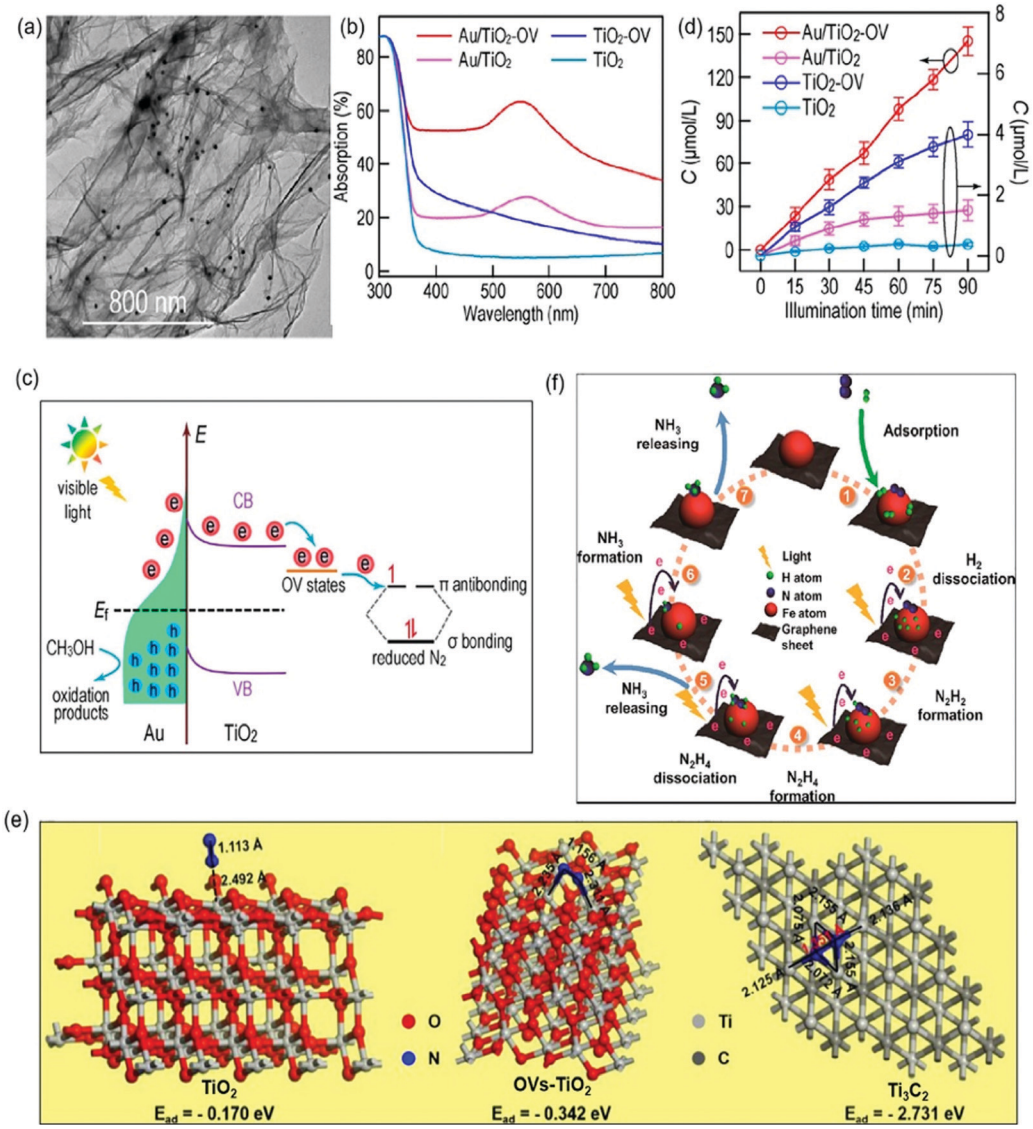

Fig. 11 (a) TEM image of Au/TiO_2-OV. (b) Adsorption spectra of different photocatalysts. (c) The proposed schematic for photocatalytic N_2 reduction over the Au/TiO_2-OV catalyst under visible-light irradiation. (d) Photocatalytic NH_3 production with different photocatalysts under visible light irradiation. Reproduced from ref. 96 with permission from ACS Publication. (e) Schematic of the adsorption structure on TiO_2 (A), OVs-TiO_2 (B) and Ti_3C_2 MXenes (C). Reproduced from ref. 103 with permission from Elsevier Publication. (f) Schematic for photocatalytic N_2 reduction over Fe@graphene photocatalysts. Reproduced from ref. 108 with permission from ACS Publication.

© 2021 The Author(s). Published by the Royal Society of Chemistry

Open Access Article. Published on 03 11 2020. Downloaded on 2025-03-11 5:25:41.
This article is licensed under a Creative Commons Attribution 3.0 Unported Licence.

photocatalytic N_2 reduction.[105] The DFT calculations revealed that the SVs and the metal properties of 1T-MoS_2 could effectively promote the separation of h^+/e^- and the presence of SV-1T-MoS_2 could also provide abundant active sites, resulting in enhanced N_2 adsorption and immobilization. Accordingly, a remarkable performance over the optimal SV-1T-MoS_2/CdS was realized with a superior NH_3 yield rate of 8220.83 μmol L^{-1} h^{-1} g^{-1} under simulated solar light irradiation. Besides, NiS was also studied as a cocatalyst over CdS nanorods for ammonia photosynthesis.[106] The DFT calculation indicated that the NiS cocatalyst could reduce the adsorption energy of N_2 from 1.16 eV on the CdS surface to −0.55 eV on the Ni-doped CdS surface. Further characterization revealed that charge separation could also be enhanced by loading NiS on the CdS surface. Because of these properties, a favorable NH_3 yield of 2.8 mg L^{-1} was reported within the first hour in pure water under full-spectrum irradiation. Recently, single-atom Pt modified triazine framework (CTF) nanosheets (Pt-SACs/CTF) were developed for photocatalytic NH_3 production.[107] It was found that the Pt–N_3 sites were formed in Pt-SACs/CTF, leading to more negative conduction band position with accelerated thermodynamics and fast interfacial charge migration ability, and therefore a high NH_3 production rate of 171.4 μmol g^{-1} h^{-1} under visible light irradiation. Most recently, we synthesized a ternary Ru/RuO_2/g-C_3N_4 system for N_2 photoreduction, which exhibited a photocatalytic NH_3 yield of 13.3 μmol g^{-1} h^{-1} whilst no NH_3 could be measured for pure g-C_3N_4 under the same condition. Such significant improvement in photocatalytic NH_3 synthesis for Ru/RuO_2/g-C_3N_4 was not only because of Ru and RuO_2 acting as cocatalysts to promote electron and hole transfer respectively, but also due to the advantage of Ru for N_2 chemisorption and activation.[108] Besides that, carbon-based materials especially graphene are also often used as cocatalysts to prevent the photoinduced electron–hole recombination and promote the electron transfer due to their prominent electrical conductivity.[109,110] For instance, a Fe modified three-dimensional graphene (Fe@graphene) photocatalyst was reported for NH_3 production.[110] In the Fe@graphene system (Fig. 11f), graphene generated hot electrons under light irradiation and transferred those electrons to Fe, while Fe acted as an electron sink and provided the catalytic active sites for the adsorption and activation of N_2.

Junction structure. The combination of two semiconductors as a photocatalyst would overcome the shortages of each component, and construct the heterostructure or Z-scheme system with improved photoelectric properties for broad applications.[111–115] In one work, Bi_2MoO_6 was implanted on g-C_3N_4 nanosheets to enhance the photocatalytic N_2 reduction.[111] In this case, the obtained g-C_3N_4/Bi_2MoO_6 heterojunction showed effective separation of charge carriers and enhanced photocatalytic performance for NH_3 production. In another report, MXene-derived TiO_2@C incorporated with g-C_3N_4 (TiO_2@C/g-C_3N_4, Fig. 12a) was prepared for efficient NH_3 photocatalysis.[112] Compared with the pristine g-C_3N_4, TiO_2@C/g-C_3N_4 showed a significantly decreased PL intensity (Fig. 12b), which indicated that the heterostructure promoted the charge transfer, which in turn inhibited the recombination of photoinduced electron–hole pairs. Furthermore, the transient photocurrent density of TiO_2@C/g-C_3N_4 was about 1.7 times higher than that of g-C_3N_4 (Fig. 12c), suggesting the improved separation efficiency of the charge carriers. The N_2-TDP result revealed that the Ti^{3+} species on TiO_2 and carbonaceous components were responsible

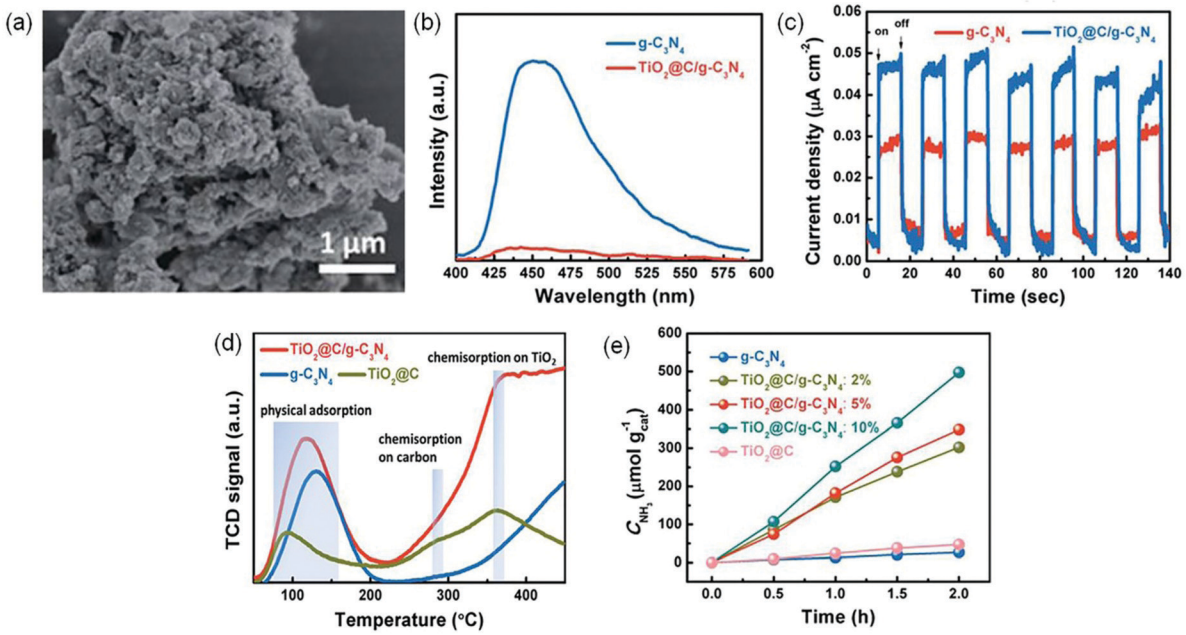

Fig. 12 (a) SEM image of TiO_2@C/g-C_3N_4. (b) PL spectra of TiO_2@C/g-C_3N_4 and g-C_3N_4. (c) Transient photocurrent responses of TiO_2@C/g-C_3N_4 and g-C_3N_4. (d) The N_2-TPD profiles. (e) The yield of produced NH_3 under visible light irradiation ($\lambda > 420$ nm). Reproduced from ref. 112 with permission from The Royal Society of Chemistry.

Open Access Article. Published on 03 11 2020. Downloaded on 2025-03-11 5:25:41.
This article is licensed under a Creative Commons Attribution 3.0 Unported Licence.

for the adsorption and activation of N_2 in TiO_2@C/g-C_3N_4 (Fig. 12d). As a result, a superior performance over the optimal TiO_2@C/g-C_3N_4:10 (10 represents the molar ratio of starting materials of melamine/Ti_3C_2) was realized with an NH_3 production yield of 250.6 μmol g^{-1} h^{-1} using methanol as a scavenger under visible light irradiation (Fig. 12e). Recently, a p–n junction of Bi_2MoO_6/OV-BiOBr combining n-type Bi_2MoO_6 nanorods with OV-rich p-type BiOBr nanosheets displayed efficient charge separation and a broad range of light absorption.[116] Moreover, OVs on the surface of Bi_2MoO_6/OV-BiOBr were beneficial for the chemisorption and activation of N_2, and the nanosheet morphology could provide a large specific surface area with more active sites for photoreduction of N_2. Benefiting from these advantages, the optimal Bi_2MoO_6/OV-BiOBr exhibited a photocatalytic yield of NH_3 of 81.0 μmol g^{-1} h^{-1} under visible light illumination in pure water, and no O_2 production was reported here.

Conclusion and perspectives

The photosynthesis of NH_3 is an energy-saving process and has high potential for substantial contribution to economic and social sustainability. Compared with the traditional Haber–Bosch process and the emerging electrochemical process, photocatalytic NH_3 synthesis exhibits very low efficiency, mostly at micromoles g^{-1} h^{-1} if using water as the electron donor, and thus is far from practical application. However as photocatalysis can be driven by abundant solar energy, it is a carbon-free process. Besides, it requires a solar energy input of 208.3 MJ kg^{-1}-NH_3 compared with that of 339.1 MJ kg^{-1}-NH_3 in the electrochemical process.[117] Thus, it has strong potential to achieve NH_3 synthesis with affordable costs in particular taking into account the sustainability and the trend of decarbonatization in the industry. However there is a long way to go in order to realize this potential.

This review does not detail different photocatalysts as there are a few reviews on them, but analyses surface engineering and interface engineering in photocatalysts developed recently for the photocatalytic NH_3 synthesis, involving oxygen vacancies, nitrogen vacancies, carbon vacancies, sulfur vacancies, metal and non-metal doping, facet modulation, nanostructure engineering, and heterostructure construction such as loading with cocatalysts and modification with other semiconductors, together with the mechanism of N_2 reduction reaction and the reliable means for the detection of NH_3.

Great progress has been made in the study of photoreduction of N_2 to NH_3 as briefed in Fig. 13, but there are still many problems, some of which are very critical. First, the majority of the studies so far reported use an efficient and expensive hole scavenger to get long lived photoelectrons for N_2 reduction. However, a practical pathway should use water as the only electron donor and to provide protons for the photosynthesis of NH_3, as such NH_3 synthesis by photocatalysis is scientifically meaningful and economically sustainable. The slow progress linked to this profile is mainly due to the very limited understanding in this field. Second, there are few reports specifying

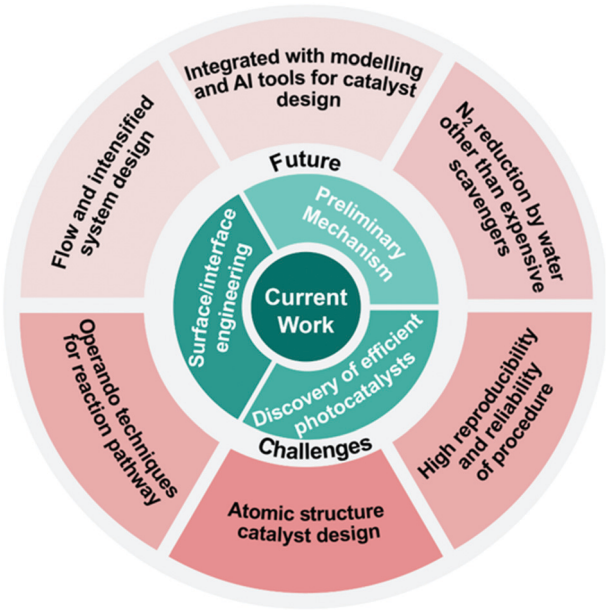

Fig. 13 Current work and future challenges highlighted in this review.

the stoichiometric chemistry in the photochemical process. Without the stoichiometric O_2 gas produced, such N_2 reduction to NH_3 is questionable. Furthermore, as O_2 could be leaked from air, the isotopic measurement of O_2 production is necessary. In addition, since H_2 production would compete with NH_3 synthesis, a comprehensive study should detail the selectivity between the two products and discuss the strategy to favor NH_3 synthesis. In addition an experimental error bar is very crucial for such NH_3 synthesis in order to improve the confidence as almost all studies were carried out in a batch reactor with quite a small amount of NH_3 produced, which was quite easy to be interfered by occasional factors.

Apart from the issues mentioned above, photocatalytic NH_3 synthesis also faces a few tough challenges. The majority of the studies show that the NH_4 amount produced is less than 10 μmol h^{-1} (instead of the unit of μmol g^{-1} h^{-1}) when using water as the electron donor and 10 times enhancement is achieved when using an organic hole scavenger. This amount is lower than the NH_3 amount in the river water which is about 0.01 mM.[118] Besides, since the NH_3 yield is extremely easy to be interfered by environmental impurities and different detection agents, it is difficult to obtain reliable and reproducible results by just one analysis method.[119] At least two methods have to be applied to prove the consistent results and to improve the reproducibility of the process.

The surface states of a catalyst can dominate its performance, such as surface defects. However, to quantify the correlation of the surface defects with the catalytic activity is very challenging at present. This should be undertaken in the future in order to distinctly guide catalyst surface state control. Furthermore the cocatalyst is another key factor to control both charge separation and catalytic performance. The majority of the cocatalysts reported are either large particles or nanosized particles. Single atomic catalysis is an emerging area, which

© 2021 The Author(s). Published by the Royal Society of Chemistry

Open Access Article. Published on 03 11 2020. Downloaded on 2025-03-11 5:25:41.
This article is licensed under a Creative Commons Attribution 3.0 Unported Licence.

presents unprecedented activity in some chemical processes. Such unique reaction sites should be introduced to ammonia synthesis with in-depth exploration of their intrinsic function. In addition, a junction structure is widely accepted to help charge separation, which was also reviewed in the previous session. The new design strategy should be applied to construct new junctions, such as polymer and oxide junctions as the former has likely better N_2 adsorption due to the potential hydrogen bond between the organic polymer and N_2 while the latter has a very positive VB for water oxidation.

The modified catalyst discovery is very informative. Equally, the mechanism and reaction pathways for photocatalytic N_2 fixation are scarce and much less investigated, forming an obstacle for the rational design of highly efficient photocatalysts. Currently, most of the given reaction mechanisms and reaction pathways were based on assumptions and lacked solid evidence. Thus, the current catalyst development is more or less a try-and-error process. Some advanced operando technologies in functional characterization should be applied to comprehensively study the reaction pathway such as by time resolved spectroscopy to investigate charge carrier dynamics, and by transient and stationary spectroscopy to observe the reaction intermediates.

In addition, it is of paramount importance to design a flow reaction system for N_2 photoreduction. The current reaction system is composed of a batch reactor, which is far from the requirement of the industry. The typical batch reactor is easy to be constructed; however, its efficiency is severely restricted by the low mass transfer between N_2 gas and aqueous solution due to the low solubility of N_2, thereby resulting in a low photocatalytic efficiency. Besides, NH_3 accumulated in the batch reactor during the reaction process will be overoxidized to other byproducts, thereby resulting in a low conversion rate and even bad selectivity. Moreover, based on the industrial viewpoint, it is quite costly to separate the photocatalysts from reactants and products in a batch system. Thus, an intensified flow reactor such as using N_2 and water vapor as reactants should be explored to overcome these drawbacks and to meet the industrial requirement in the future, underlining the crucial collaborations between chemical scientists and experts in reaction engineering.

Last, modelling will be expected to combine with experimental results to figure out the reaction mechanism and speed up the rational design of highly efficient photocatalysts. Meanwhile, the big data, together with artificial intelligence (AI) and machine learning (ML), will be a future key research area to improve the reproducibility of the catalyst synthesis, to facilitate catalyst screening, to enhance the experimental safety and to save the experimental costs and time.

Overall, this research field is at an infant state and all these areas should be enhanced in order to improve the NH_3 synthesis rate with high reproducibility and reliability of the procedure.

Conflicts of interest

There are no conflicts to declare.

Acknowledgements

Q. H. is thankful for the NSFC grants (21575014 and 21905025), Beijing Natural Science Foundation (2184122), the Fundamental Research Funds for the Central Universities (2018CX01017), Beijing Institute of Technology Research Fund Program for Young Scholars, and Analysis & Testing Center at Beijing Institute of Technology. H.M.J is thankful for the UCL Dean's prize and China CSC scholarship. All authors are thankful for financial support from UK EPSRC (EP/N009533/1), Royal Society-Newton Advanced Fellowship Grant (NA170422) and the Leverhulme Trust (RPG-2017-122).

References

1 V. Smil, *Nature*, 1999, **400**, 415.
2 H. P. Jia and E. A. Quadrelli, *Chem. Soc. Rev.*, 2014, **43**, 547–564.
3 K. Ithisuphalap, H. Zhang, L. Guo, Q. Yang, H. Yang and G. Wu, *Small Methods*, 2019, **3**, 1800352.
4 G. Ertl, *Angew. Chem., Int. Ed.*, 2008, **47**, 3524–3535.
5 R. Schlögl, *Angew. Chem., Int. Ed.*, 2003, **42**, 2004–2008.
6 C. Mao, J. Wang, Y. Zou, H. Li, G. Zhan, J. Li, J. Zhao and L. Zhang, *Green Chem.*, 2019, **21**, 2852–2867.
7 P. Wang, F. Chang, W. Gao, J. Guo, G. Wu, T. He and P. Chen, *Nat. Chem.*, 2017, **9**, 64–70.
8 N. Cherkasov, A. O. Ibhadon and P. Fitzpatrick, *Chem. Eng. Process.*, 2015, **90**, 24–33.
9 G. Duan, Y. Chen, Y. Tang, K. A. M. Gasem, P. Wan, D. Ding and M. Fan, *Prog. Energy Combust. Sci.*, 2020, **81**, 100860.
10 R. Zhao, H. Xie, L. Chang, X. Zhang, X. Zhu, X. Tong, T. Wang, Y. Luo, P. Wei, Z. Wang and X. Sun, *EnergyChem*, 2019, **1**, 100011.
11 S. C. Sun, X. Y. Zhang, X. L. Liu, L. Pan, X. W. Zhang and J. J. Zou, *Acta Phys.-Chim. Sin.*, 2020, **36**, 1905007.
12 Y. Zhao, R. Shi, X. Bian, C. Zhou, Y. Zhao, S. Zhang, F. Wu, G. I. N. Waterhouse, L. Z. Wu, C. H. Tung and T. Zhang, *Adv. Sci.*, 2019, **6**, 1802109.
13 Y. Huang, N. Zhang, Z. Wu and X. Xie, *J. Mater. Chem. A*, 2020, **8**, 4978–4995.
14 A. J. Medford and M. C. Hatzell, *ACS Catal.*, 2017, **7**, 2624–2643.
15 C. Guo, J. Ran, A. Vasileff and S. Z. Qiao, *Energy Environ. Sci.*, 2018, **11**, 45–56.
16 Y. J. Zhang, F. X. Mao, L. J. Wang, H. Y. Yuan, P. F. Liu and H. G. Yang, *Sol. RRL*, 2020, **4**, 1900438.
17 G. N. Schrauzer and T. D. Guth, *J. Am. Chem. Soc.*, 1977, **99**, 7189–7193.
18 M. Cheng, C. Xiao and Y. Xie, *J. Mater. Chem. A*, 2019, **7**, 19616–19633.
19 D. Yan, H. Li, C. Chen, Y. Zou and S. Wang, *Small Methods*, 2019, **3**, 1800331.
20 S. Zhang, Y. Zhao, R. Shi, C. Zhou, G. I. N. Waterhouse, L. Z. Wu, C. H. Tung and T. Zhang, *Adv. Energy Mater.*, 2020, **10**, 1901973.

Open Access Article. Published on 03 11 2020. Downloaded on 2025-03-11 5:25:41.
This article is licensed under a Creative Commons Attribution 3.0 Unported Licence.

21 Y. Zhao, R. Shi, X. Bian, C. Zhou, Y. Zhao, S. Zhang, F. Wu, G. I. N. Waterhouse, L. Z. Wu, C. H. Tung and T. Zhang, *Adv. Sci.*, 2019, **6**, 1802109.
22 X. Chen, N. Li, Z. Kong, W. J. Ong and X. Zhao, *Mater. Horiz.*, 2018, **5**, 9–27.
23 X. Xue, R. Chen, H. Chen, Y. Hu, Q. Ding, Z. Liu, L. Ma, G. Zhu, W. Zhang, Q. Yu, J. Liu, J. Ma and Z. Jin, *Nano Lett.*, 2018, **18**, 7372–7377.
24 X. Y. Xie, P. Xiao, W.-H. Fang, G. Cui and W. Thiel, *ACS Catal.*, 2019, **9**, 9178–9187.
25 A. J. Medford and M. C. Hatzell, *ACS Catal.*, 2017, **7**, 2624–2643.
26 J. Li, H. Li, G. Zhan and L. Zhang, *Acc. Chem. Res.*, 2017, **50**, 112–121.
27 M. A. Shipman and M. D. Symes, *Catal. Today*, 2017, **286**, 57–68.
28 C. Ling, Y. Zhang, Q. Li, X. Bai, L. Shi and J. Wang, *J. Am. Chem. Soc.*, 2019, **141**, 18264–18270.
29 X. Gao, Y. Wen, D. Qu, L. An, S. Luan, W. Jiang, X. Zong, X. Liu and Z. Sun, *ACS Sustainable Chem. Eng.*, 2018, **6**, 5342–5348.
30 A. Banerjee, B. D. Yuhas, E. A. Margulies, Y. Zhang, Y. Shim, M. R. Wasielewski and M. G. Kanatzidis, *J. Am. Chem. Soc.*, 2015, **137**, 2030–2034.
31 H. Li, J. Shang, Z. Ai and L. Zhang, *J. Am. Chem. Soc.*, 2015, **137**, 6393–6399.
32 H. Hirakawa, M. Hashimoto, Y. Shiraishi and T. Hirai, *J. Am. Chem. Soc.*, 2017, **139**, 10929–10936.
33 C. Li, T. Wang, Z. J. Zhao, W. Yang, J.-F. Li, A. Li, Z. Yang, G. A. Ozin and J. Gong, *Angew. Chem., Int. Ed.*, 2018, **57**, 5278–5282.
34 Y. Zhao, X. Jia, G. I. N. Waterhouse, L.-Z. Wu, C. H. Tung, D. O'Hare and T. Zhang, *Adv. Energy Mater.*, 2016, **6**, 1501974.
35 S. Zhang, Y. Zhao, R. Shi, C. Zhou, G. I. N. Waterhouse, L. Z. Wu, C. H. Tung and T. Zhang, *Adv. Energy Mater.*, 2020, **10**, 1901973.
36 Y. Zhao, Y. Zhao, G. I. N. Waterhouse, L. Zheng, X. Cao, F. Teng, L. Z. Wu, C. H. Tung, D. O'Hare and T. Zhang, *Adv. Mater.*, 2017, **29**, 1703828.
37 L. Ye, L. Zan, L. Tian, T. Peng and J. Zhang, *Chem. Commun.*, 2011, **47**, 6951–6953.
38 H. Li and L. Zhang, *Nanoscale*, 2014, **6**, 7805–7810.
39 J. Chen, T. Ding, J. Cai, Y. Wang, M. Wu, H. Zhang, W. Zhao, Y. Tian, X. Wang and X. Li, *Appl. Surf. Sci.*, 2018, **453**, 101–109.
40 Y. Wang, J. Cai, M. Wu, J. Chen, W. Zhao, Y. Tian, T. Ding, J. Zhang, Z. Jiang and X. Li, *Appl. Catal., B*, 2018, **239**, 398–407.
41 Y. Huang, Y. Yu, Y. Yu and B. Zhang, *Sol. RRL*, 2020, **4**, 2000037.
42 Q. Han, B. Wang, J. Gao, Z. Cheng, Y. Zhao, Z. Zhang and L. Qu, *ACS Nano*, 2016, **10**, 2745–2751.
43 Q. Han, Z. Cheng, B. Wang, H. Zhang and L. Qu, *ACS Nano*, 2018, **12**, 5221–5227.
44 H. Ou, L. Lin, Y. Zheng, P. Yang, Y. Fang and X. Wang, *Adv. Mater.*, 2017, **29**, 1700008.
45 Q. Han, B. Wang, J. Gao and L. Qu, *Angew. Chem., Int. Ed.*, 2016, **55**, 10849–10853.
46 Q. Han, B. Wang, Y. Zhao, C. Hu and L. Qu, *Angew. Chem., Int. Ed.*, 2015, **54**, 11433–11437.
47 Y. Liang, F. Liu, Y. Deng, Q. Zhou, Z. Cheng, P. Zhang, Y. Xiao, L. Lv, H. Liang, Q. Han, H. Shao and L. Qu, *Small*, 2018, **14**, 1801916.
48 Q. Han, C. Hu, F. Zhao, Z. Zhang, N. Chen and L. Qu, *J. Mater. Chem. A*, 2015, **3**, 4612–4619.
49 L. Chen, Y. Wang, C. Wu, G. Yu, Y. Yin, C. Su, J. Xie, Q. Han and L. Qu, *Nanoscale*, 2020, **12**, 13484–13490.
50 Q. Han, N. Chen, J. Zhang and L. Qu, *Mater. Horiz.*, 2017, **4**, 832–850.
51 B. He, M. Feng, X. Chen and J. Sun, *Green Energy Environ.*, 2020, DOI: 10.1016/j.gee.2020.07.011.
52 Y. Wang and S. Shen, *Acta Phys.-Chim. Sin.*, 2020, **36**, 1905080.
53 W. J. Ong, L. K. Putri and A. R. Mohamed, *Chem. – Eur. J.*, 2020, **26**, 9710–9748.
54 G. Dong, W. Ho and C. Wang, *J. Mater. Chem. A*, 2015, **3**, 23435–23441.
55 W. Wang, H. Zhang, S. Zhang, Y. Liu, G. Wang, C. Sun and H. Zhao, *Angew. Chem., Int. Ed.*, 2019, **11**, 16644–16650.
56 S. Cao, B. Fan, Y. Feng, H. Chen, F. Jiang and X. Wang, *Chem. Eng. J.*, 2018, **353**, 147–156.
57 Y. Cao, S. Hu, F. Li, Z. Fan, J. Bai, G. Lu and Q. Wang, *RSC Adv.*, 2016, **6**, 49862–49867.
58 V. Kumaravel, S. Mathew, J. Bartlett and S. C. Pillai, *Appl. Catal., B*, 2019, **244**, 1021–1064.
59 Z. Shayegan, C. S. Lee and F. Haghighat, *Chem. Eng. J.*, 2018, **334**, 2408–2439.
60 J. J. Carey and M. Nolan, *J. Mater. Chem. A*, 2017, **5**, 15613–15630.
61 Y. Shi, Y. Zhou, D. R. Yang, W. X. Xu, C. Wang, F. B. Wang, J. J. Xu, X.-H. Xia and H. Y. Chen, *J. Am. Chem. Soc.*, 2017, **139**, 15479–15485.
62 E. Paek, A. J. Pak and G. S. Hwang, *ACS Appl. Mater. Interfaces*, 2014, **6**, 12168–12176.
63 J. Zhang, Y. Liu, C. Sun, P. Xi, S. Peng, D. Gao and D. Xue, *ACS Energy Lett.*, 2018, **3**, 779–786.
64 W. Zhao, J. Zhang, X. Zhu, M. Zhang, J. Tang, M. Tan and Y. Wang, *Appl. Catal., B*, 2014, **144**, 468–477.
65 J. Luo, X. Bai, Q. Li, X. Yu, C. Li, Z. Wang, W. Wu, Y. Liang, Z. Zhao and H. Liu, *Nano Energy*, 2019, **66**, 104187.
66 N. Zhang, L. Li, Q. Shao, T. Zhu, X. Huang and X. Xiao, *ACS Appl. Energy Mater.*, 2019, **2**, 8394–8398.
67 N. Zhang, A. Jalil, D. Wu, S. Chen, Y. Liu, C. Gao, W. Ye, Z. Qi, H. Ju, C. Wang, X. Wu, L. Song, J. Zhu and Y. Xiong, *J. Am. Chem. Soc.*, 2018, **140**, 9434–9443.
68 Y. Zhao, Y. Zhao, R. Shi, B. Wang, G. I. N. Waterhouse, L. Z. Wu, C. H. Tung and T. Zhang, *Adv. Mater.*, 2019, **31**, 1806482.
69 Y. Bi, S. Ouyang, N. Umezawa, J. Cao and J. Ye, *J. Am. Chem. Soc.*, 2011, **133**, 6490–6492.
70 P. V. Kamat, *Acc. Chem. Res.*, 2017, **50**, 527–531.
71 Q. Hao, C. Liu, G. Jia, Y. Wang, H. Arandiyan, W. Wei and B. J. Ni, *Mater. Horiz.*, 2020, **7**, 1014–1029.

© 2021 The Author(s). Published by the Royal Society of Chemistry

Open Access Article. Published on 03 11 2020. Downloaded on 2025-03-11 5:25:41.
This article is licensed under a Creative Commons Attribution 3.0 Unported Licence.

72 Z. Li, Z. Gao, B. Li, L. Zhang, R. Fu, Y. Li, X. Mu and L. Li, *Appl. Catal., B*, 2020, **262**, 118276.
73 W. Wang, H. Zhou, Y. Liu, S. Zhang, Y. Zhang, G. Wang, H. Zhang and H. Zhao, *Small*, 2020, **16**, 1906880.
74 M. Setvin, X. Hao, B. Daniel, J. Pavelec, Z. Novotny, G. S. Parkinson, M. Schmid, G. Kresse, C. Franchini and U. Diebold, *Angew. Chem., Int. Ed.*, 2014, **53**, 4714–4716.
75 J. Bai, B. Lu, Q. Han, Q. Li and L. Qu, *ACS Appl. Mater. Interfaces*, 2018, **10**, 38066–38072.
76 G. Liu, J. C. Yu, G. Q. Lu and H. M. Cheng, *Chem. Commun.*, 2011, **47**, 6763–6783.
77 Y. Bai, L. Ye, T. Chen, L. Wang, X. Shi, X. Zhang and D. Chen, *ACS Appl. Mater. Interfaces*, 2016, **8**, 27661–27668.
78 H. Li, J. Shang, J. Shi, K. Zhao and L. Zhang, *Nanoscale*, 2016, **8**, 1986–1993.
79 Q. Han, Z. Cheng, J. Gao, Y. Zhao, Z. Zhang, L. Dai and L. Qu, *Adv. Funct. Mater.*, 2017, **27**, 1606352.
80 Y. O. Wang, F. Silveri, M. K. Bayazit, Q. S. Ruan, Y. M. Li, J. J. Xie, C. R. A. Catlow and J. W. Tang, *Adv. Energy Mater.*, 2018, **8**, 1801084.
81 Q. Han, F. Zhao, C. Hu, L. Lv, Z. Zhang, N. Chen and L. Qu, *Nano Res.*, 2015, **8**, 1718–1728.
82 J. Bai, Q. Han, Z. Cheng and L. Qu, *Chem. – Asian J.*, 2018, **13**, 3160–3164.
83 L. W. Chen, X. T. Ding, J. F. Zeng, C. B. Wu, Q. Han and L. T. Qu, *Sci. Bull.*, 2019, **54**, 718–722.
84 Y. Wang, R. Xu, L. Chen, C. Wu, L. Qiu, C. D. Windle, Q. Han and L. Qu, *ACS Appl. Mater. Interfaces*, 2020, **12**, 8547–8554.
85 G. Zhang, C. D. Sewell, P. Zhang, H. Mi and Z. Lin, *Nano Energy*, 2020, **71**, 104645.
86 S. Sun, Q. An, W. Wang, L. Zhang, J. Liu and W. A. Goddard III, *J. Mater. Chem. A*, 2017, **5**, 201–209.
87 S. Wang, X. Hai, X. Ding, K. Chang, Y. Xiang, X. Meng, Z. Yang, H. Chen and J. Ye, *Adv. Mater.*, 2017, **29**, 1701774.
88 S. Bian, M. Wen, J. Wang, N. Yang, P. K. Chu and X. F. Yu, *J. Phys. Chem. Lett.*, 2020, **11**, 1052–1058.
89 L. Lin, Q. Zhu, A. Cheng and L. Ma, *Catal. Sci. Technol.*, 2020, **10**, 4119–4125.
90 J. Ran, J. Zhang, J. Yu, M. Jaroniec and S. Z. Qiao, *Chem. Soc. Rev.*, 2014, **43**, 7787–7812.
91 R. Li, H. Han, F. Zhang, D. Wang and C. Li, *Energy Environ. Sci.*, 2014, **7**, 1369–1376.
92 G. Zhang, Z. A. Lan and X. Wang, *Chem. Sci.*, 2017, **8**, 5261–5274.
93 K. T. Ranjit, T. K. Varadarajan and B. Viswanathan, *J. Photochem. Photobiol., A*, 1996, **96**, 181–185.
94 Q. Zhang and J. Guan, *Sol. RRL*, 2020, **4**, 2000283.
95 S. Liu, Y. Wang, S. Wang, M. You, S. Hong, T. S. Wu, Y. L. Soo, Z. Zhao, G. Jiang, Q. Jieshan, B. Wang and Z. Sun, *ACS Sustainable Chem. Eng.*, 2019, **7**, 6813–6820.
96 J. Yang, Y. Guo, R. Jiang, F. Qin, H. Zhang, W. Lu, J. Wang and J. C. Yu, *J. Am. Chem. Soc.*, 2018, **140**, 8497–8508.
97 R. Wang, T. Xie, Z. Sun, T. Pu, W. Li and J.-P. Ao, *RSC Adv.*, 2017, **7**, 51687–51694.
98 X. W. Guo, S. M. Chen, H. J. Wang, Z. M. Zhang, H. Lin, L. Song and T. B. Lu, *J. Mater. Chem. A*, 2019, **7**, 19831–19837.
99 S. Chang and X. Xu, *Inorg. Chem. Front.*, 2020, **7**, 620–624.
100 J. Wang, C. Hua, X. Dong, Y. Wang and N. Zheng, *Sustainable Energy Fuels*, 2020, **4**, 1855–1862.
101 J. J. Xie, R. Jin, A. Li, Q. Ruan, Y. Deng, Y. Zhang, S. Yao, G. Sankar, D. Ma and J. W. Tang, *Nat. Catal.*, 2018, **11**, 889–896.
102 J. Yang, D. Wang, H. Han and C. Li, *Acc. Chem. Res.*, 2013, **46**, 1900–1909.
103 Y. Liao, J. Qian, G. Xie, Q. Han, W. Dang, Y. Wang, L. Lv, S. Zhao, L. Luo, W. Zhang, H.-Y. Jiang and J. Tang, *Appl. Catal., B*, 2020, **273**, 119054.
104 C. M. Janet, S. Navaladian, B. Viswanathan, T. K. Varadarajan and R. P. Viswanath, *J. Phys. Chem. C*, 2010, **114**, 2622–2632.
105 B. Sun, Z. Liang, Y. Qian, X. Xu, Y. Han and J. Tian, *ACS Appl. Mater. Interfaces*, 2020, **12**, 7257–7269.
106 X. Gao, L. An, D. Qu, W. Jiang, Y. Chai, S. Sun, X. Liu and Z. Sun, *Sci. Bull.*, 2019, **64**, 918–925.
107 J. Li, P. Liu, Y. Tang, H. Huang, H. Cui, D. Mei and C. Zhong, *ACS Catal.*, 2020, **10**, 2431–2442.
108 H. Wang, X. Li, Q. Ruan and J. Tang, *Nanoscale*, 2020, **12**, 12329–12335.
109 S. X. Wang, H. Maimaiti, B. Xu, Y. Guo, P. S. Zhai and H. Z. Zhang, *J. Phys. Chem. C*, 2019, **123**, 31119–31129.
110 Y. Lu, Y. Yang, T. Zhang, Z. Ge, H. Chang, P. Xiao, Y. Xie, L. Hua, Q. Li, H. Li, B. Ma, N. Guan, Y. Ma and Y. Chen, *ACS Nano*, 2016, **10**, 10507–10515.
111 E. Vesali-Kermani, A. Habibi-Yangjeh, H. Diarmand-Khalilabad and S. Ghosh, *J. Colloid Interface Sci.*, 2020, **563**, 81–91.
112 Q. Liu, L. Ai and J. Jiang, *J. Mater. Chem. A*, 2018, **6**, 4102–4110.
113 H. Mou, J. Wang, D. Zhang, D. Yu, W. Chen, D. Wang and T. Mu, *J. Mater. Chem. A*, 2019, **7**, 5719–5725.
114 W. J. Ong and K. P. Y. Shak, *Sol. RRL*, 2020, **4**, 2000132.
115 W. Zhang, A. R. Mohamed and W. J. Ong, *Angew. Chem., Int. Ed.*, 2020, DOI: 10.1002/anie.201914925.
116 X. Xue, R. Chen, C. Yan, Y. Hu, W. Zhang, S. Yang, L. Ma, G. Zhu and Z. Jin, *Nanoscale*, 2019, **11**, 10439–10445.
117 L. Wang, M. Xia, H. Wang, K. Huang, C. Qian, C. T. Maravelias and G. A. Ozin, *Joule*, 2018, **2**, 1055–1074.
118 S. Gandaseca, N. Rosli, J. Ngayop and C. Arianto, *Am. J. Environ. Sci.*, 2011, **7**, 269–275.
119 S. Z. Andersen, V. Čolić, S. Yang, J. A. Schwalbe, A. C. Nielander, J. M. McEnaney, K. Enemark-Rasmussen, J. G. Baker, A. R. Singh, B. A. Rohr, M. J. Statt, S. J. Blair, S. Mezzavilla, J. Kibsgaard, P. C. K. Vesborg, M. Cargnello, S. F. Bent, T. F. Jaramillo, I. E. L. Stephens, J. K. Nørskov and I. Chorkendorff, *Nature*, 2019, **570**, 504–508.

© 2021 The Author(s). Published by the Royal Society of Chemistry